Search for $B^- \to \Lambda_c^+ \bar{p} \ell^- \bar{\nu}_\ell$ decays at Belle II

Tim Müller

Masterarbeit in Physik
angefertigt im Physikalischen Institut

vorgelegt der
Mathematisch-Naturwissenschaftlichen Fakultät
der
Rheinischen Friedrich-Wilhelms-Universität
Bonn

July 2026

I hereby declare that this thesis was formulated by myself and that no sources or tools other than those cited were used.

Bonn, 13.07.2026 .... Date

T. Müller .... Signature

Gutachter und Betreuer: Dr. Markus Prim
Gutachter: Prof. Dr. Florian Bernlochner

Abstract

This thesis presents a study of the rare baryonic semileptonic decay $B^- \to \Lambda_c^+ \bar{p} \ell^- \bar{\nu}_\ell$, with $\ell = e, \mu$, using simulated Belle II data. This decay is expected to contribute dominantly to the baryonic component of the inclusive semileptonic decay rate and may therefore help clarify the origin of the long-standing problem of the semileptonic gap. The signal is reconstructed using the hadronic tagging technique, while dedicated selection criteria are developed to suppress continuum and generic $B\bar{B}$ backgrounds. Several veto strategies targeting intermediate Σ_c resonances are investigated and validated. Although these vetoes successfully reject dedicated background samples, they are found to reduce the overall signal significance because of the large combinatorial background in $B\bar{B}$ events and are therefore not applied for the final results. The signal extraction is performed using a binned maximum-likelihood template fit to the missing mass squared distribution. Statistical and systematic uncertainties arising from Monte Carlo statistics, hadronic tag calibration, tracking efficiency and particle identification are incorporated as nuisance parameters. Based on Asimov data sets, no significant signal excess is expected and upper limits at the 90 % confidence level are determined. For the combined electron and muon channels, an upper limit of $\mathcal{B}(B^- \to \Lambda_c^+ \bar{p} \ell^- \bar{\nu}_\ell) < 4.3 \times 10^{-6}$ is obtained, while separate limits of 5.2×10^{-6} and 9.4×10^{-6} are derived for the electron and muon channels, respectively. These results demonstrate the expected sensitivity of the Belle II experiment to this rare baryonic semileptonic decay and provide an important foundation for future analyses using recorded collision data.

Contents

CHAPTER 1

Introduction

The Standard Model of Particle Physics is currently the most successful and precise theory of fundamental physics, describing the elementary particles and their interactions. Its predictions have been confirmed by numerous experimental measurements with extraordinary precision. However, some observations remain unexplained, suggesting this model to be incomplete. Consequently, one of the primary goals of modern particle physics is to search for deviations from the Standard Model of Particle Physics through increasingly precise experimental measurements.

An important testing ground is flavour physics, where transitions between different quark flavours are described by the Cabbibo-Kobayashi-Maskawa matrix. Precise determinations of its matrix elements allow stringent tests of its unitarity and therefore of the Standard Model of Particle Physics itself. In particular, semileptonic decays of B mesons provide access to the determination of the matrix element $|V_{cb}|$. However, one long-standing problem arises from a discrepancy between the measured inclusive semileptonic branching fraction and the sum of all experimentally established exclusive decay modes, commonly referred to as the "semileptonic gap". This discrepancy suggests that a fraction of semileptonic decays proceeds through final states that have not yet been measured precisely. Among the most promising candidates are baryonic semileptonic B decays, whose experimental reconstruction is considerably more challenging than that of mesonic final states.

This thesis focuses on the search for the decay

$$B^- \to \Lambda_c^+ \bar{p} \ell^- \bar{\nu}_\ell,$$

with $\ell = e, \mu$, which is expected to be the dominant baryonic semileptonic decay of the B meson. A measurement of its branching fraction would improve our understanding of the baryonic contribution to the inclusive semileptonic decay rate and may help explain part of the semileptonic gap. In the long term, such measurements contribute to more precise determinations of $|V_{cb}|$ and thereby strengthen tests of the Standard Model of Particle Physics.

The analysis presented in this thesis is performed within the Belle II experiment at the SuperKEKB asymmetric e^+e^- collider. The decay is reconstructed using the hadronic tagging method, allowing the presence of the undetected neutrino to be inferred from the missing momentum of the event. Various event selections are developed to suppress different background sources and the remaining signal contribution is extracted using a binned maximum-likelihood template fit. The expected sensitivity is evaluated by incorporating statistical and systematic uncertainties into the statistical model, and an upper limit on the branching fraction is determined.

Therefore this thesis is structured as follows. Chapter 2 introduces the theoretical framework relevant for this analysis, describing the Standard Model of Particle Physics and motivating the study of the semileptonic baryonic B decays. Chapter 3 presents the SuperKEKB collider with the Belle II detector. The reconstruction of the signal decay and applied event selections are described in chapter 4. Remaining background contributions and how they can be further suppressed are showcased in chapter 5. Finally, chapter 6 discusses the statistical analysis, including the template fit, the treatment of systematic uncertainties and the determination of the upper limit on the branching fraction.

Throughout this thesis, natural units with $\hbar = c = 1$ are used unless stated otherwise.

CHAPTER 2

The Standard Model of Particle Physics

The Standard Model of Particle Physics (SM) provides a remarkably successful theoretical framework describing the fundamental constituents of matter and their interactions. Within this framework, all known elementary particles are classified as fermions or bosons, whose behaviour is governed by underlying gauge symmetries. Its theory is based on the gauge group $SU(3)_C \times SU(2)_L \times U(1)_Y$, which describes strong and electroweak interactions. Through spontaneous breaking of the electroweak symmetry, the electromagnetic interaction emerges from this theory [1]. Over the last decades its predictions have been extensively tested in a wide range of experiments and has demonstrated excellent agreement with observations across many energy scales [2–4]. With the discovery of the Higgs boson in 2012 [5] the particle spectrum predicted by the model was completed and the mechanism responsible for mass generation of elementary particles was confirmed. Nevertheless, several open questions remain unresolved, including the asymmetry between matter and antimatter, the nature of dark matter and the dynamics governing hadron formation through weak decays.

In figure 2.1 the SM is depicted with its elementary particles, their basic characteristics and classifications, which will be further explained in the next sections.

2.1 Elementary Particles

All known elementary particles can be divided into two main categories: fermions, which form matter, and bosons, which mediate interactions. Both are described in the following and is based on [7].

2.1.1 Fermions

Fermions are particles with spin-$\frac{1}{2}$, which are arranged in three generations. Each generation consists of two quarks and two leptons. Quarks possess fractional electric charge and appear in the pairs up and down, charm and strange and top and bottom. Additionally, they carry colour charge and are therefore affected by all interactions of the SM. Quarks cannot be observed as free particles due to colour confinement but instead combine to form hadrons such as mesons and baryons. Leptons consist of the charged particles electrons, muons and tauons and their corresponding neutrinos. These charged leptons interact via electromagnetic and weak interactions, while neutrinos are chargeless and interact only through the weak interaction. Particles belonging to higher generations are heavier and are most likely to decay into lighter particles through weak processes.

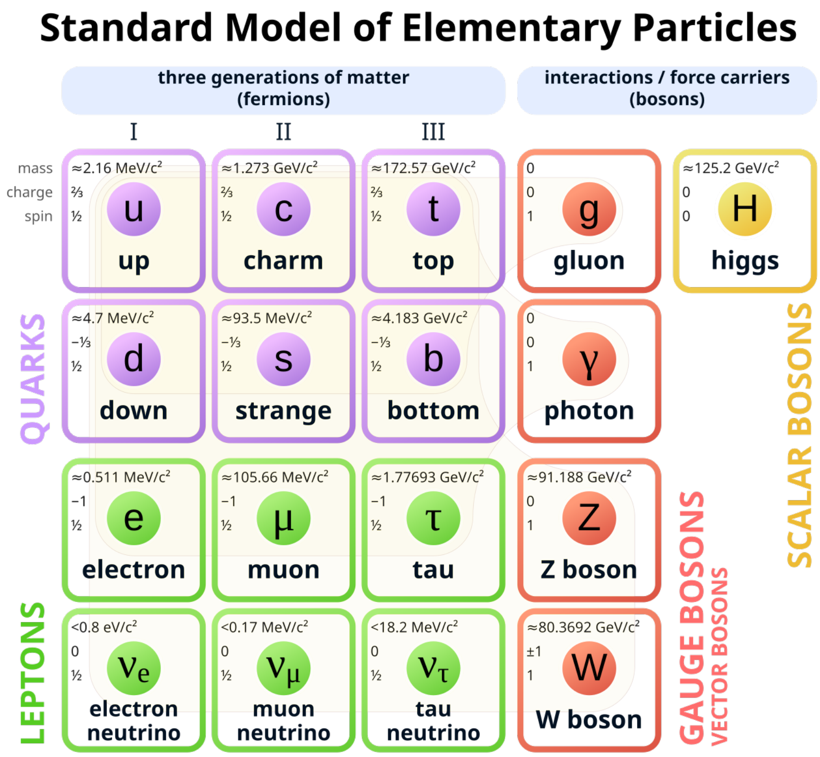

Figure 2.1: The Structure of the Standard Model of Particle Physics with its components is shown. The different types of elementary particles can be seen in different colours, where the fermions are sorted in three generations with increasing mass. To every particle the mass, charge and spin is mentioned. [6]

2.1.2 Bosons

Interactions between fermions are carried by gauge bosons, which have a spin of 1. The electromagnetic interaction is governed by the photon and the strong interaction by gluons, both having no electrical charge and no mass. Lastly, the weak interaction is mediated by the charged W boson and the neutral Z boson with a relatively high mass of 80 GeV and 91 GeV respectively. Masses of elementary particles arise through the Higgs mechanism. The Higgs field permeates space and the coupling of particles to this field generates their mass. The associated excitation of this field is the Higgs boson, whose discovery confirmed this mechanism of the SM experimentally. It is a particle with spin of 0, no electrical charge and a mass of around 125 GeV.

2.2 Fundamental Interactions

The strong interaction is described by Quantum Chromodynamics (QCD) and acts between quarks through the exchange of gluons. Two main properties characterise this interaction: confinement and asymptotic freedom. Confinement ensures that quarks are bound or confined at low energies for example inside hadrons, while asymptotic freedom implies that quarks behave nearly as free particles at very high energies. The electromagnetic interaction governs processes involving electrically charged particles and is mediated by photons. It is described by Quantum Electrodynamics (QED), one of the most precisely tested theories in physics. The weak interaction is responsible for flavour-changing processes and particle decays. It is mediated by the massive W and Z bosons and uniquely violates parity symmetry. In the quark sector, flavour transitions are described by the CKM matrix, which introduces mixing between quark generations and provides a source of charge-parity (CP) violation. [7]

2.3 The CKM Matrix

As previously stated, the Cabbibo-Kobayashi-Maskawa (CKM) matrix describes the transitions between different quark flavours. It is depicted in 2.1, where V_{ij} are the matrix elements that define the relative strength of the interaction between the quarks i and j. The matrix can also be rewritten into the second expression, namely the Wolfenstein parametrisation, with the small parameter $\lambda = \sin\theta_c = 0.225$ and the three other real parameters A, ρ and η [8]. The angle θ_c is here the Cabibbo angle.

$$V_{CKM} = \begin{pmatrix} V_{ud} & V_{us} & V_{ub} \\ V_{cd} & V_{cs} & V_{cb} \\ V_{td} & V_{ts} & V_{tb} \end{pmatrix} = \begin{pmatrix} 1-\lambda^2/2 & \lambda & A\lambda^3(\rho - i\eta) \\ -\lambda & 1-\lambda^2/2 & A\lambda^2 \\ A\lambda^3(1-\rho-i\eta) & -A\lambda^2 & 1 \end{pmatrix} + O(\lambda^4) \tag{2.1}$$

The values for $|V_{ij}|$ can be separately determined by measuring different decays, for example the matrix element $|V_{ud}| = \cos\theta_c = 0.97425$ can be derived from β-decays. This leads to the approximate matrix values shown in 2.2. [7]

$$\begin{pmatrix} |V_{ud}| & |V_{us}| & |V_{ub}| \\ |V_{cd}| & |V_{cs}| & |V_{cb}| \\ |V_{td}| & |V_{ts}| & |V_{tb}| \end{pmatrix} \approx \begin{pmatrix} 0.974 & 0.225 & 0.004 \\ 0.225 & 0.973 & 0.041 \\ 0.009 & 0.040 & 0.999 \end{pmatrix} \tag{2.2}$$

In the SM the CKM matrix is unitary, meaning the condition $V^\dagger V = I$ is met, which imposes $\sum_i V_{ij}V^*_{ik} = \delta_{jk}$ and $\sum_j V_{ij}V^*_{kj} = \delta_{ik}$. The six combinations that equal to zero can be represented as triangles in a complex plane. The most commonly used unitarity triangle arises from the relation

$$V_{ud}V^*_{ub} + V_{cd}V^*_{cb} + V_{td}V^*_{tb} = 0, \tag{2.3}$$

by dividing both sides of the equation by the best-known term, $V_{cd}V^*_{cb}$. The vertices are in (0,0), (1,0) and $(\bar{\rho}, \bar{\eta})$, where $\bar{\rho} = \rho(1 - \lambda^2/2 + \ldots)$ and $\bar{\eta} = \eta(1 - \lambda^2/2 + \ldots)$. The resulting unitarity triangle can be seen in figure 2.2. The shape of the triangle is determined solely by the parameters $\bar{\rho}$ and $\bar{\eta}$. By precisely measuring independent observables sensitive to different CKM elements, the unitarity triangle can be overconstrained. Within the SM all flavour measurements must correspond to a single consistent triangle. [9]

The results of a global fit to all available measurements, determining the CKM matrix elements, and constraints on the $\bar{\rho}, \bar{\eta}$ plane from various experiments are depicted in figure 2.3. The shaded regions corresponding to different measurements overlap in a common area, demonstrating the overall consistency of current flavour data with the SM prediction. Any measurement deviating significantly from this region could hint at physics beyond the SM.

Crucially, the precision of this test relies on accurate determinations of the CKM matrix elements that define the sides of the triangle, in particular $|V_{cb}|$ and $|V_{ub}|$, which are predominantly extracted

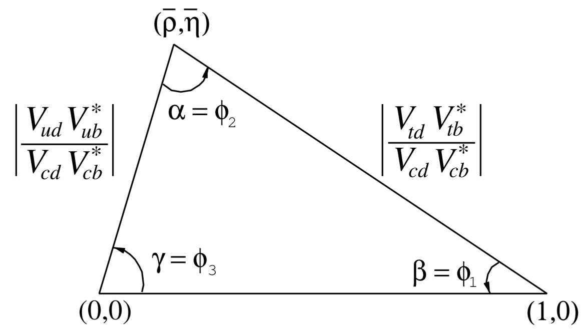

Figure 2.2: A sketch of the unitarity triangle derived from the CKM matrix is shown. The vertices are located at (0,0) and (1,0), which are fixed, and at $(\bar{\rho}, \bar{\eta})$, which depends on the angles and the sides of the triangle. The sides of the triangle depend here on multiple CKM matrix elements. [9]

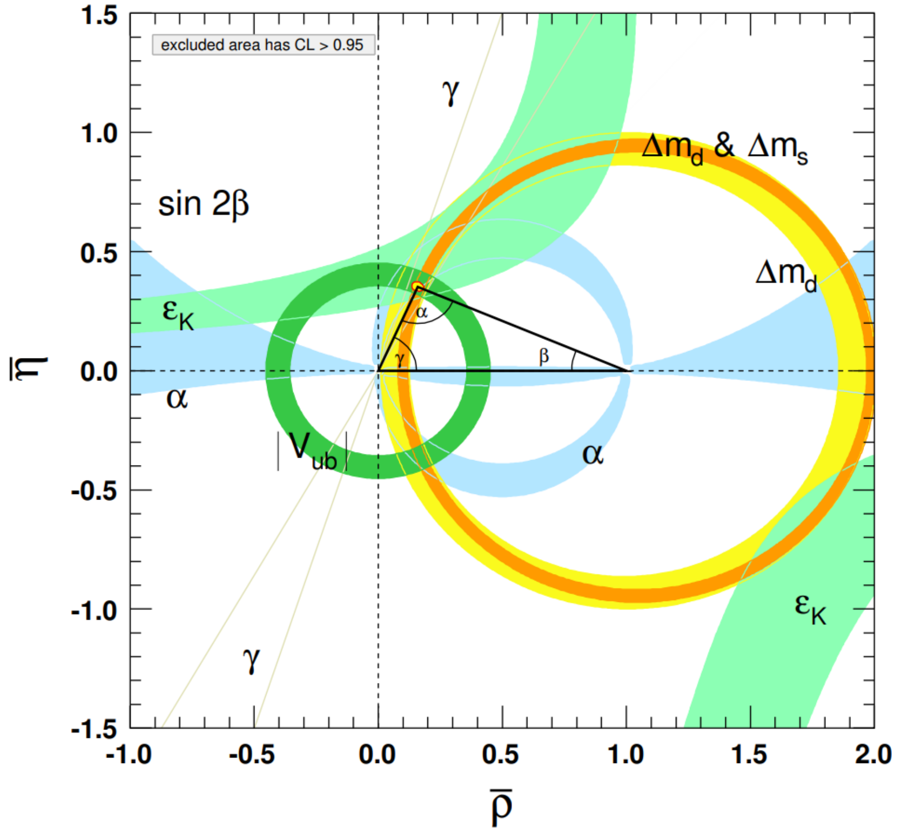

Figure 2.3: Multiple constraints on the $\bar{\rho}, \bar{\eta}$ plane can be seen in different colours. All these constraints consistently overlap in the vertex $(\bar{\rho}, \bar{\eta})$ of the triangle, providing a test of the Standard Model of Particle Physics. [9]

from semileptonic B meson decays. A detailed understanding of these decays is therefore essential for advancing precision tests of the flavour sector. [9]

2.4 Testing the Standard Model

Although highly successful, the SM cannot be considered a complete theory of fundamental physics. Several experimental observations cannot be explained within its framework, indicating the existence of physics beyond the SM. Among the most prominent examples are the existence of dark matter [10], the origin of neutrino masses [11], the matter-antimatter asymmetry of the universe [12] and the absence of a quantum description of gravity [13]. While these observations motivate the search for new physics, no direct production of particles beyond the SM has been established so far. An alternative and highly complementary approach therefore consist of performing precision measurements of processes that are accurately predicted by the SM. Even small deviations between experimental measurements and theoretical predictions may reveal contributions from virtual particles or interactions that are inaccessible through direct searches.

As discussed in the previous section, flavour physics offers one of the most powerful laboratories for such precision tests with the CKM matrix. Its unitarity allows the construction of the unitarity triangle, whose sides and angles can be determined from a variety of independent decay processes. Within the SM, all of these measurements must be consistent with a single unitary CKM matrix. Any statistically significant inconsistencies would therefore indicate either an incomplete theoretical description of the underlying hadronic dynamics or contributions beyond the SM. The precision of these tests is limited not only by the experimental uncertainties but also by how accurately the individual CKM matrix elements can be determined. In particular, the matrix element $|V_{cb}|$, which normalises two sides of the unitarity triangle, is primarily extracted from semileptonic decays of B mesons with $b \to c$ processes. [9]

The decay rate of semileptonic $b \to c$ transitions is proportional to $|V_{cb}|^2$. Because the leptonic current is fully described by the electroweak interaction, theoretical uncertainties are largely confined to the hadronic transition. Semileptonic decays therefore provide one of the cleanest environments for determining $|V_{cb}|$ and testing the flavour sector of the SM. The semileptonic B decay into D^0 is an example of such decays used to determine $|V_{cb}|$ and its feynman diagram is shown in figure 2.4.

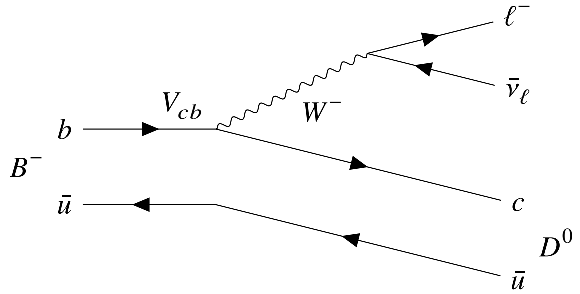

Figure 2.4: Tree-level Feynman diagram of the quark-level transition $b \to cW^-$ underlying the semileptonic decay $B^- \to D^0\ell^-\bar{\nu}_\ell$. The matrix element V_{cb} can be determined from decays like that.

The hadronic transition between the initial B meson and the final state charmed hadron is governed by non-perturbative QCD effects. These effects are parametrized by hadronic form factors, which describe the overlap of the hadronic wave functions and depend on the squared four momentum transfer q^2 of the virtual W boson. Since these form factors cannot be calculated reliably using perturbative QCD, they have to be obtained from non-perturbative approaches such as lattice QCD, Heavy-Quark Effective Theory (HQET) or light cone sum rules [14]. However, in this analysis the signal Monte Carlo samples were generated according to a pure phase-space (PHSP) model. Consequently, no specific form factor parametrization was assumed in the event generation, making this analysis largely model independent with respect to the decay dynamics [15].

A long-standing challenge in determining $|V_{cb}|$ is the discrepancy between the inclusive and exclusive measurements of semileptonic B decays, commonly referred to as the "semileptonic gap". Inclusive measurements consider the total decay rate of all possible semileptonic processes

$$B \to X_c \ell \nu,$$

where X_c denotes any charmed hadronic final state. This branching fraction is experimentally and theoretically well understood and is determined to be

$$\mathcal{B}(B \to X_c \ell \nu) = (10.63 \pm 0.15)\,\%. \tag{2.4}$$

In contrast, exclusive measurements reconstruct specific decay channels like $B \to D \ell \nu$, $B \to D^* \ell \nu$ or $B \to D^{**} \ell \nu$. Summing up the branching fractions of these decays with a D meson in the final state only result in a branching fraction of

$$\mathcal{B}(B \to D X \ell \nu) = (9.47 \pm 0.27)\,\%, \tag{2.5}$$

resulting in an unaccounted gap of $(1.16 \pm 0.31)\,\%$ [16]. This discrepancy indicates that a fraction of the inclusive semileptonic decay rate originates from experimentally challenging final states that have not yet been sufficiently explored. While mesonic final states have been studied extensively [17–19], contributions from more complex hadronic systems, in particular baryonic final states, remain poorly constrained. Baryonic semileptonic decays exhibit lower reconstruction efficiencies, larger combinatorial backgrounds and significantly smaller branching fractions, making them considerably more difficult to study experimentally. Nevertheless, they are expected to contribute to the inclusive semileptonic decay rate and are therefore of particular importance for solving the semileptonic gap. A precise investigation of baryonic semileptonic decays not only improves our understanding of the hadronization process in weak $b \to c$ transitions but also helps to clarify the origin of the missing branching fraction. Ultimately, this contributes to a more precise determination of $|V_{cb}|$, strengthens global CKM unitarity tests and thereby improves the sensitivity for flavour physics to possible contributions from physics beyond the SM.

2.5 The Decay $B^- \to \Lambda_c^+ \bar{p} \ell^- \bar{\nu}_\ell$

Among the possible baryonic semileptonic decays, the channel

$$B^- \to \Lambda_c^+ \bar{p} \ell^- \bar{\nu}_\ell \tag{2.6}$$

is of special interest. It represents the lightest accessible final state containing a charmed baryon and is expected to be the dominant baryonic semileptonic mode, while also being the simplest baryon-antibaryon production in a $b \to c$ transition. Measuring its branching fraction therefore directly probes the baryonic contribution to the inclusive semileptonic decay rate and provides valuable information for resolving the semileptonic gap.

At the quark level, the decay proceeds through the tree level charged current transition $b \to cW^-$, followed by the leptonic decay $W^- \to \ell^- \bar{\nu}_\ell$. Since the process occurs already at tree level in the SM, large deviations from the predicted decay rate are not generally expected. Nevertheless, precision measurements of rare semileptonic decays provide sensitive probes of possible contributions from physics beyond the SM through modifications of the charged current interaction. Various extensions of the SM, including models with charged Higgs bosons, heavy W' bosons or leptoquarks, may introduce additional charged current mediators, which could modify the decay amplitude, branching fraction or differential decay distributions [20]. Although the present analysis is not designed to search directly for such effects, precise measurements or limits on rare semileptonic decay help constrain these scenarios.

Previous searches by the CLEO and BaBar collaboration [21–23] established experimental strategies but did not yield a definitive measurement of this channel. The present analysis constitutes the first direct measurement of $B^- \to \Lambda_c^+ \bar{p} \ell^- \bar{\nu}_\ell$ at Belle II. By determining an upper limit on its branching fraction this study aims to improve our understanding of baryonic semileptonic B decays, provide input towards resolving the semileptonic gap and contribute to future precision determinations of $|V_{cb}|$. Ultimately, a precise measurement of this decay would improve the knowledge of the exclusive semileptonic decay composition, thereby strengthening CKM-based tests of the SM.

The unprecedented luminosity delivered by the B-factory SuperKEKB, together with the advanced reconstruction capabilities of the Belle II detector enable the study of rare decay modes such as $B^- \to \Lambda_c^+ \bar{p} \ell^- \bar{\nu}_\ell$ with significant improvements to the sensitivity. The SuperKEKB collider and Belle II experiment will be presented in the following chapter.

CHAPTER 3

SuperKEKB and the Belle II experiment

The detection of the semileptonic decay $B^- \to \Lambda_c^+ \bar{p} \ell^- \bar{\nu}_\ell$ and measurement of its branching fraction requires large samples of B mesons produced under well controlled experimental conditions. Electron-positron colliders operating at the $\Upsilon(4S)$ resonance provide an ideal environment for this purpose, as they enable clean production of $B\bar{B}$ pairs with low background contributions. The SuperKEKB collider delivers such conditions by colliding high-intensity electron and positron beams at unprecedented luminosities. The particles produced in these collisions are recorded by the Belle II detector, a general purpose spectrometer designed to measure different parameters like energy and momentum of charged and neutral particles with high precision. Belle II is the successor of the Belle detector, which was operated at the KEKB collider between 1998 and 2010 and was significantly upgraded to cope with the higher luminosity and increased background levels of SuperKEKB [24]. This chapter gives an overview of the SuperKEKB collider, describing its characteristics and beam production, as well as the Belle II detector with its components.

3.1 SuperKEKB

SuperKEKB is an asymmetric electron-positron collider located at the High Energy Accelerator Research Organization (KEK) in Tsukuba, Japan. The accelerator has been operating since 2018 and represents the next-generation B factory, designed to deliver extremely high luminosities for precision studies of heavy-flavour physics. The instantaneous luminosity is a metric for the collision rate at a collider and can be expressed as

$$L = \frac{N_b n_{e^-} n_{e^+} f}{A_{\text{eff}}}, \tag{3.1}$$

where N_b is the number of bunches, $n_{e^\pm}$ the number of positrons or electrons in a bunch, f the revolution frequency and A_{eff} the effective transverse overlap of the colliding beams [25]. Integrating the instantaneous luminosity over time yields the integrated luminosity,

$$L_{\text{int}} = \int L(t)\, dt, \tag{3.2}$$

which quantifies the total size of the collected data set. This metric also gives the expected number of events N for a process with cross section σ_{cross} with $N = \sigma_{\text{cross}} \cdot L_{\text{int}}$. The cross section is a measure for the quantum mechanical probability of the specific interaction. [7]

With a circumference of approximately 3 km, SuperKEKB succeeds its predecessor, the KEKB collider, and provides significantly increased collision rates required for rare decay measurements and searches for physics beyond the Standard Model. [26]

3.1.1 Characteristics of the collider

The collider consists of two independent storage rings in which electrons and positrons circulate in opposite directions. Electrons are accelerated in the High Energy Ring (HER) to an energy of 7 GeV, while positrons are stored in the Low Energy Ring (LER) at 4 GeV. The asymmetric beam energies produce a Lorentz boost of the Centre-of-Mass System (CMS) along the beam axis. This boost allows spatial separation between the decay vertices of the two produced B mesons, which is essential for precision measurements of decay dynamics and time-dependent observables.

To achieve the required collision rates, SuperKEKB employs the so-called nano-beam scheme. A large crossing angle between the two beams at the interaction point (IP), combined with strong focusing of the beams to nanometer-scale, significantly increases the particle density at the collision point. This approach drastically reduces the effective collision area A_{eff} of the two beams from formula 3.1, thus increasing the luminosity. The collider therefore aims to reach a design instantaneous luminosity of

$$\mathcal{L} = 8 \times 10^{35}\,\text{cm}^{-2}\,\text{s}^{-1},$$

corresponding to an improvement by roughly a factor of 40 compared to its predecessor.

SuperKEKB operates primarily at the energy of the $\Upsilon(4S)$ resonance, a $b\bar{b}$ bound state with a CMS energy of

$$\sqrt{s} = 10.58\,\text{GeV}.$$

The $\Upsilon(4S)$ decays almost exclusively into $B\bar{B}$ meson pairs produced nearly at rest in the CMS. This clean production mechanism, together with the precisely known initial state of electron-positron collisions, makes SuperKEKB an ideal environment for precision measurements of B meson decays. For this reason, the facility is commonly referred to as a B factory. [24]

3.1.2 Structure and beam production

A schematic overview of the collider is shown in Figure 3.1. Beam production begins at the Linear Accelerator (LINAC), which serves as the injector system for both storage rings. Electrons are generated by an electron gun located at the beginning of the LINAC. These electrons are accelerated to high energies using radio-frequency (RF) accelerating cavities. On the other hand, positrons are produced indirectly: accelerated electrons from the LINAC are directed onto a target material, where electromagnetic showers generate electron-positron pairs. The resulting positrons are collected, focused, and subsequently accelerated within the LINAC.

After acceleration, the particle beams are transferred into damping rings that reduce beam emittance by decreasing transverse momentum spread. Low emittance beams are essential for achieving the small beam sizes required by the nano-beam scheme. The beams are then injected into their respective storage

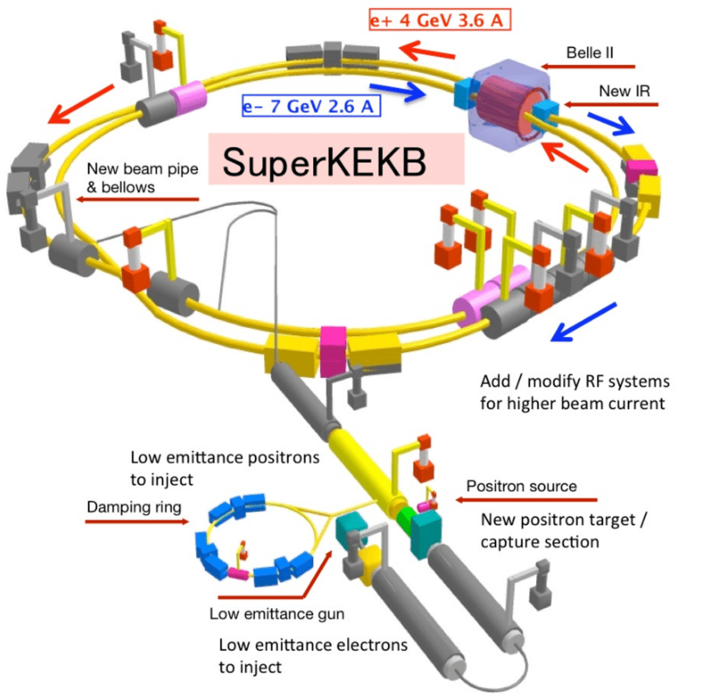

Figure 3.1: Schematic overview of the SuperKEKB collider. At the bottom the components for the beam production can be found, leading to the two storage rings. The two beams accelerate to different energies and collide at the top right Belle II detector. [27]

rings, the HER for electrons and the LER for positrons, where they circulate for many hours while continuously replenished through top-up injection.

Within the storage rings, superconducting RF cavities compensate for energy losses due to synchrotron radiation and maintain stable beam currents. A system of bending magnets guides the beams along the circular trajectory, while quadrupole and sextupole magnets focus and stabilize the beam optics. Near the point of collision, strong final-focus magnets compress the beams to nanometer-scale dimensions before collision. [28]

The electron and positron beams intersect at the IP, where the Belle II detector is located.

3.2 The Belle II detector

Due to the increased luminosities of the SuperKEKB the detector also needed to be upgraded to detect and process higher amounts of data. It consists of multiple detector components, which are cylindrically arranged around the beamline at the IP. These different components provide various information about the detected particles like energy, momentum and charge. Combining these information makes it possible to identify and calculate properties of the produced particles and decay processes. The entire detector is 10 m high and wide and weighs in total 1500 tons. [29]

The onion-like structure of the detector with its different components is shown in figure 3.2. Particle detectors at collider experiments are typically divided into geometrical regions according to their

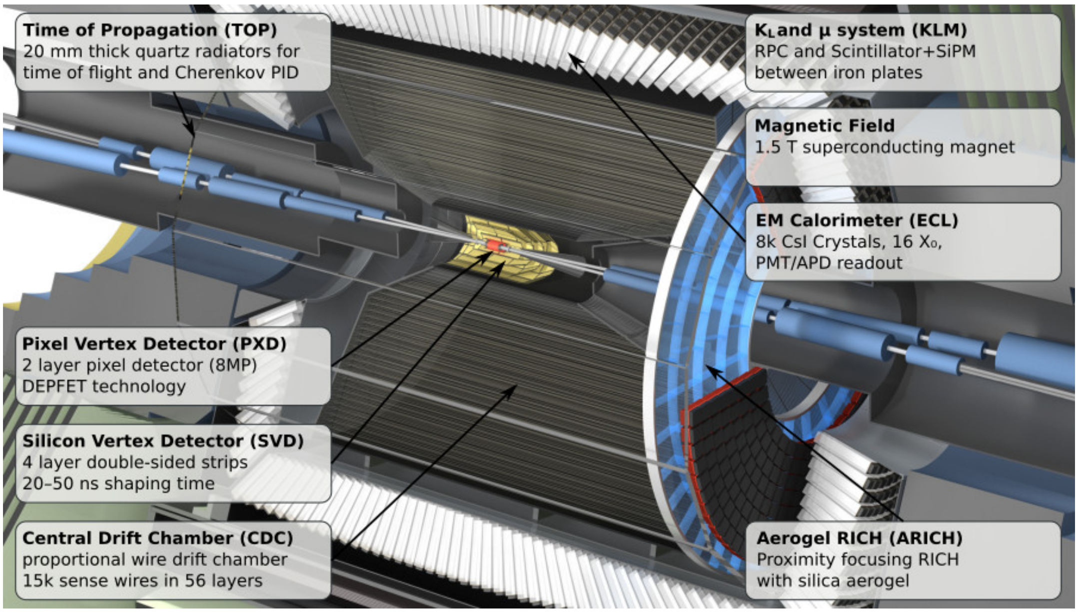

Figure 3.2: The onion-like structure of the Belle II detector is depicted. Each subdetector is shown with a short description. [29]

orientation with respect to the beam axis. The cylindrical symmetry of electron-positron collisions naturally leads to the distinction between barrel and end-cap regions. The barrel region refers to the central cylindrical part of the detector surrounding the IP and oriented perpendicular to the beam axis. The forward and backward end-cap regions are located at the two ends of the detector along the beam axis. These regions detect particles produced at small polar angles relative to the incoming beams. The forward end-cap corresponds to the direction of the electron beam, while the backward end-cap covers the opposite direction.

This and the following sections are based on information provided in [28, 30], unless stated otherwise.

3.2.1 Vertex Detector System

The high-resolution Vertex Detector System (VXD) is the innermost subdetector system and consists of the Pixel Vertex Detector (PXD) and Silicon Vertex Detector (SVD), shown in the picture 3.2 as the orange and yellow components, respectively. Two layers of pixelated silicon sensors form the PXD, which is surrounded by four layers of double-sided silicon strip sensors constituting the SVD. This system is used to measure decay vertex positions of short-lived particle decays in the order of picoseconds, such as those of the B mesons or charmed hadrons. It achieves high spatial resolution resulting in precise reconstruction of decay vertices.

3.2.2 Central Drift Chamber

After passing through the VXD the produced particles travel through the Central Drift Chamber (CDC), which is the tracking detector for Belle II. A superconducting solenoid coil surrounding most of the detector system[1] produces a uniform magnetic field of 1.5 T, causing the trajectories of charged particles to curve thanks to the Lorentz force. Simultaneously, charged particles ionize the low density gas mixture inside the CDC so detectable traces are generated, enabling precise trajectory and momentum measurements. Additionally, the CDC provides particle identification information using measurements of energy loss $\frac{\mathrm{d}E}{\mathrm{d}x}$ within its gas volume. The CDC is essential for reconstructing charged decay products such as protons, kaons, and pions produced for example in Λ_c^+ decays.

3.2.3 Time of Propagation Detector

In the barrel region time of propagation (TOP) counters provide particle identification of high momentum particles using quartz radiator bars located on the outer wall of the CDC. Charged particles emit Cherenkov photons in a cone shape when traversing through the radiator bars with a higher velocity than the speed of light in that material. Concurrently, the Cherenkov angle of the cone depends on the velocity of the particle. The produced photons are internally reflected inside the quartz bars until reaching a photomultiplier (PMT), where the time of propagation is measured to determine the angle of the Cherenkov cone and therefore the particles velocity.

3.2.4 Aerogel Ring-Imaging Cherenkov detector

In the forward end-cap region, particle identification for high momentum particles is performed by the Aerogel Ring-Imaging Cherenkov detector (A-RICH). Similar to the TOP detector, charged particles produce Cherenkov photons when passing through the two aerogel radiator layers when the velocity is higher than the speed of light in the aerogel material. The emission of Cherenkov photons cause ring-like patterns in the detector plane where the radius directly correlates to the velocity of the charged particle.

3.2.5 Electromagnetic Calorimeter

Electromagnetically interacting particles like photons and electrons are mainly detected in the Electromagnetic Calorimeter (ECL). It is comprised of 8736 CsI(Tl) scintillator crystals in the barrel region, as well as the forward and backward end-cap region. When electrons interact with the calorimeter material, they produce scintillation light via Bremsstrahlung or through Coulomb interactions, resulting in ionization and atomic excitation. Photons must first undergo a direct interaction like pair production or Compton Scattering to produce secondary electrons. The scintillation light is then captured, amplified, and analyzed to reconstruct the energy. The ECL plays a central role in electron identification, reconstruction of neutral pions through photon pairs and determination of the total visible energy in an event. Accurate energy measurements are particularly important for semileptonic analyses, where missing energy is used to infer the presence of neutrinos.

3.2.6 K_L and μ system System

The outermost subsystem of Belle II is the K_L and μ system (KLM) system, located outside the superconducting solenoid. It consists of alternating layers of active detector elements and iron plates, which also serve as a magnetic flux return for the solenoid. The KLM identifies penetrating particles such as muons and long-lived neutral kaons. Muons and non-showering charged hadrons must possess a

[1] all components except the KLM

momentum of at least $|\vec{p}| = 0.6\,\mathrm{GeV}$ to reach the KLM. Since it is located outside the solenoid, these particles follow nearly straight trajectories until exiting the system or depositing their energy due to electromagnetic interactions. K_L mesons may produce hadronic showers in the ECL or the iron plates of the KLM, which can be detected in the ECL, KLM or in both.

3.2.7 Particle Identification

The information provided by the individual Belle II subdetectors in sections **??** is used to identify the different particles. For a given reconstructed charged track, each relevant subdetector contributes a likelihood L_i for a specific mass hypotheses i, where i may correspond to a final state particle like electron, muon, pion, kaon or proton. The product of these individual likelihoods from the different subdetectors result in a combined likelihood. A likelihood ratio (PID) may be constructed to give a quantitative measure of the probability that a track corresponds to the hypothesis i:

$$P_i = \frac{\mathcal{L}_i}{\mathcal{L}_i + \Sigma_{j \neq i} \mathcal{L}_j}. \tag{3.3}$$

In global PID the remaining particle hypotheses serve as alternatives j, giving the variables `electronID` or `muonID`, which will be used later in section 4.4.1. [31]

A particle's mass, and therefore its identity, can be inferred with its measured momentum and one additional observable: its velocity, ionization energy loss or total deposited energy. Information about the velocity are obtained from either the time of propagation in the TOP detector or the Cherenkov angle in the A-RICH. These provide the strongest separation power for high momentum tracks. For lower momenta, PID is dominated by the ionization energy loss measured in the CDC. Finally, the total electromagnetic energy in the ECL distinguishes electrons with their characteristic shower profiles clearly from hadrons.

CHAPTER 4

Event Reconstruction and Signal Selection

To investigate the semileptonic decay $B^- \to \Lambda_c^+ \bar{p} \ell^- \bar{\nu}_\ell$, this analysis is performed exclusively on Monte Carlo simulated data. These data samples are first introduced as well as the hadronic tagging technique, which is used in the reconstruction process of the event. Afterwards, the reconstruction of the signal- and tag-side B mesons are presented. Multiple selections are applied to the samples to enhance signal events over the background and the resulting missing mass squared distributions will be presented as the fitting variable of hadronic tagging.

4.1 Monte Carlo Data Samples

As mentioned before, only simulated Monte Carlo (MC) data samples are used for this analysis. The simulation sample consists of dedicated signal MC, generic $B\bar{B}$ background and continuum events. The dedicated signal MC sample was produced specifically for the decay $B^- \to \Lambda_c^+ \bar{p} \ell^- \bar{\nu}_\ell$ and consists of $N_{\text{gen}} = 8.0 \times 10^7$ generated events, divided equally into decays involving an electron or a muon. As mentioned in section 2.4, the signal events were generated using a PHSP decay model, in which final state particles are distributed uniformly over the available kinematic phase space without assuming a specific model for the decay dynamics or hadronic form factors [15]. After the Belle II skimming procedure, approximately $N_{\text{skim}} = 1.9 \times 10^7$ signal events remain in the signal MC sample and are used throughout this analysis. Skimming at Belle II is a loose preselection to reduce the data size of the sample while retaining the majority of the relevant events [32]. This equals to a skim efficiency of approximately $\epsilon_{\text{skim}} = N_{\text{skim}}/N_{\text{gen}} = 0.2369$ for the dedicated signal MC sample. A branching fraction of the signal decay is assumed to be

$$\mathcal{B}_{\text{assumed}}(B^- \to \Lambda_c^+ \bar{p} \ell^- \bar{\nu}_\ell) = 2.5 \times 10^{-5}$$

throughout the entire analysis, which is used for the normalization of the simulated signal sample. This value provides a realistic signal yield for the expected sensitivity study and is chosen to be consistent with the order of magnitude observed for related baryonic B meson decays involving a Λ_c, whose branching fractions are typically found at the level of a few 10^{-5} [33, 34]. The statistical methodology and final upper limit obtained in section 6.5 is independent of this assumption. The Λ_c is an intermediate state and thus decays further into other particles that can be detected. In this analysis, only its dominant decay mode into a proton, kaon and pion is considered for the reconstruction. Consequently, the normalization of the signal sample accounts for the corresponding branching fraction $\mathcal{B}(\Lambda_c^+ \to pK^-\pi^+) = 6.24\,\%$, which is consistent with the world average $(6.3 \pm 0.5)\,\%$[35]. To study the background contributions, generic $B\bar{B}$ MC samples are used, containing all known charged and neutral B meson decay modes, as well as continuum MC samples describing non-resonant $e^+e^- \to q\bar{q}(q = u, d, s, c)$ background, which will be further analysed in chapter 5. Both of these background samples are already skimmed and correspond to an integrated luminosity of $L_{\text{int}} = 1429.226\,\text{fb}^{-1}$. To evaluate the expected sensitivity, all simulated samples are normalized to a target data set corresponding to $N_{B\bar{B}} = 365 \times 10^6$ produced $B\bar{B}$ pairs. The dedicated signal MC sample, together with the generic $B\bar{B}$ and continuum samples, are taken from the Belle II MC16rd production campaign.

All statistical studies, including the template fit and the determination of the upper limit of the branching fraction, described in chapter 6, are performed using Asimov data sets. The Asimov data set is pseudo data with their observed counts set to be equal to the MC data to represent the expected behaviour of measured data. In the histograms of the rest of this analysis, the MC statistical uncertainty as well as statistical uncertainties of the Asimov data will be shown. Asimov data is expected to follow a Poisson distribution and thus has a statistical error of $\sigma_{\text{stat}} = \sqrt{N}$ with the entries N in the considered bin. Since the MC data consists of three separate samples its statistical uncertainty is calculated via $\sigma_{\text{stat}} = \sqrt{\Sigma_i w_i^2 N_i}$, where w_i is the scaling and N_i is the number of entries of the considered bin of the three individual samples. Hence the statistical uncertainty of the MC and the Asimov data are different depending on the calculated scaling of the different samples.

4.2 Tagging

The semileptonic decay $B^- \to \Lambda_c^+\bar{p}\ell^-\bar{\nu}_\ell$ includes an undectable neutrino in the final state. As a consequence, the signal B meson cannot be fully reconstructed from its visible decay products alone. For that reason, the accompanying B meson, denoted as B_{tag}, produced in the $e^+e^- \to \Upsilon(4S) \to B\bar{B}$ process is also reconstructed to recover this information. This method is called "tagging" and there are two different types, depending on the particles in the final state of the B_{tag}: semileptonic tagging with at least one lepton-neutrino pair or hadronic tagging with only hadrons. In this analysis hadronic tagging will be used due to its high purity. Figure 4.1 illustrates the typical event topology of the researched decay. As described before, the B meson with the wanted decay products is denoted as B_{sig} on the signal-side of the $\Upsilon(4S)$ event, while the second B meson is reconstructed independently and referred to as the tag-side B_{tag}. The remaining particles in the event are used to determine missing momentum and improve background suppression, as it will be discussed in section 5.1.

4.3 Modes of Reconstruction

The signal decay is reconstructed through the semileptonic channel depicted in equation 2.6. Since the neutrino escapes detection, only the charged final state particles are reconstructed explicitly. As mentioned before in section 4.1, the Λ_c^+ baryon is an intermediate state, further decaying into other final state particles. Only the decay $\Lambda_c^+ \to pK^-\pi^+$ is considered in this analysis within an invariant mass window. The invariant mass is a Lorentz-invariant quantity obtained from the four-momenta of the decay products and is therefore independent of the reference frame. For a system of particles the invariant

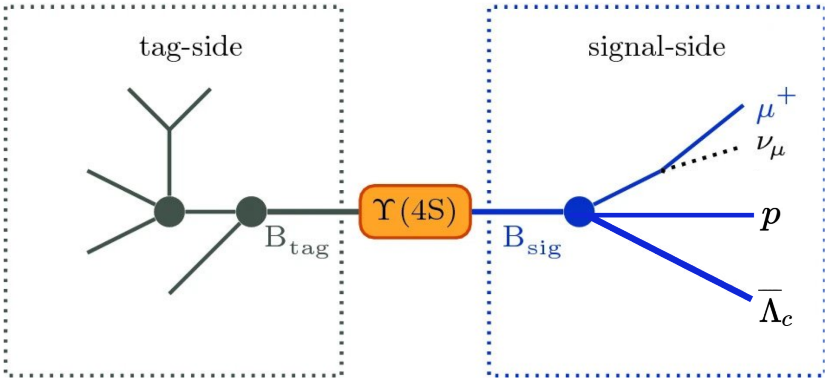

Figure 4.1: A schematic overview of a reconstructed event topology is shown. On the right one can see an example signal decay of the signal-side B meson, while on the left the decay of the accompanying B meson is depicted. (based on [36])

mass is defined as

$$M = \sqrt{\left(\Sigma E_i\right)^2 - \left|\Sigma \vec{p}_i\right|^2}, \tag{4.1}$$

where E_i and $\vec{p}_i$ denote the energy and momentum of the individual particles [7, 32]. If the selected particles originate from the decay of an intermediate resonance, the reconstructed invariant mass peaks around the mass of the parent particle. Random combinations of unrelated particles form a broad combinatorial background instead.

The resulting Λ_c^+ candidate is further combined with a lepton and proton candidate to complete the reconstruction of the B_{sig} meson. The lepton candidates are in this case an electron or muon and need to be well-defined through application of PID with momenta $p > 0.3\,\text{GeV}$. Therefore, the signal-side reconstruction follows

$$B^-_{\text{sig}} \to (\Lambda_c^+ \to pK^-\pi^+)\bar{p}\ell^-\bar{\nu}_\ell, \quad \ell = e, \mu, \tag{4.2}$$

including its charge conjugation.

The signal-side reconstruction is combined with a hadronically reconstructed tag-side B meson, allowing the use of kinematic constraints provided by the known initial state of the e^+e^- collision.

4.4 Reconstruction of Event Candidates

After the reconstruction of charged particles and intermediate states, signal candidates are formed by combining a Λ_c^+, $\bar{p}$ and charged lepton candidate. The tag-side B meson will be required to only decay into hadrons. Finally the signal and tag B mesons are combined to create $\Upsilon(4S)$ candidates. The applied selections are displayed for signal and tag B mesons, as well as $\Upsilon(4S)$ separately. All selection criteria for the complete data set and the electron or muon channel are shown in table A.3 and A.4 in the appendix. They are sorted in order of application on the data set with the number of events, multiplicity, signal efficiency and background efficiency after each selection. Multiplicity means here the average number of candidates per event and the efficiencies of signal and background are the number of events after the selection divided by the number of events before the selection:

$$\epsilon_{\mathrm{sig}} = \frac{n_{\mathrm{sig}}^{\mathrm{after}}}{n_{\mathrm{sig}}^{\mathrm{before}}} \qquad \text{and} \qquad \epsilon_{\mathrm{bkg}} = \frac{n_{\mathrm{bkg}}^{\mathrm{after}}}{n_{\mathrm{bkg}}^{\mathrm{before}}}. \tag{4.3}$$

The selections on the respective variables are also shown in the graphs A.1-A.6 in the appendix. Every graph is based on the respective data set with the applied selections from the graphs before, resulting in the final event selection.

The information about the variables that are introduced in the following are based on the Belle II Physics Book [30], unless stated otherwise.

4.4.1 Signal B Reconstruction

Signal event candidates are first selected through reconstruction of the B_{sig} from the interaction of final state particles with the Belle II detector, as discussed in section 3.2. This reconstruction is described in the following.

Charged tracks are required to originate close to the interaction point (IP) and have detectable trajectories. This includes having a polar angle within CDC acceptance, the number of hits in the CDC over 20, the specific particle probability as described in section 3.2.7 over 0.5, a transverse distance from the IP of less than 0.5 cm and a point of closest approach of the IP of less than 2 cm. These tracks are referred to as "good tracks" [32]. To reconstruct the Λ_c candidates all potential unique combinations of the four-momenta of proton, kaon and pion candidates, which are all required to be "good tracks", are summed together. The invariant mass of the Λ_c candidates additionally has to be within the window $(2.1 < M_{\Lambda_c} < 2.5)$ GeV. Furthermore, the signal B meson is reconstructed in the two decay channels shown in equation 4.2 by summing up the four-momenta of the Λ_c, proton and electron or muon candidates. For that the proton candidates, as well as the electrons and muons are also required to be "good tracks". PID selections will be applied to the lepton signatures and their momentum is required to be greater than 0.3 GeV in the lab frame. This lower momentum threshold is placed to ensure sufficient statistics for PID corrections. The PID for leptons is performed by calculating a probability from individual likelihoods based on information from the different subdetectors [32]. For electrons primary features like E/p come from the ECL, while muons are mainly defined in the KLM. Both electron and muon candidates are required to have a higher binary probability of 0.9 to reduce misidentification.

The reconstructed B_{sig} undergoes a simultaneous vertex fit to the whole reconstructed decay chain shown in equation 4.2. The best decay vertex positions and momenta are determined by converging the four-momenta of the daughter particles onto a common point. No mass constraints are applied to the final state particles. The fitting is performed by varying the four-momenta of the respective daughters, within measurement uncertainties, such that other constraints like a IP constrain are fulfilled [32]. The resulting best values of the varied momentum are used to compute the corresponding χ^2, which encodes the quality of the fit. For this analysis, the confidence level is kept at 0 % to only reject the candidates where the fit failed and the fitted values for momenta and vertex position of all daughter particles will be updated.

After the vertex fit, event-level shape quantities like Fox Wolfram moments are calculated, to make these variables accessible. Fox Wolfram moments are mathematical variables describing the geometric shape of particle collisions. They can range from 0 for spherical events like signal B decays, to 1 for jet-like continuum background events. For a collection of N particles, the l-th order Fox-Wolfram moment is defined as

$$H_l = \sum_{i,j}^{N} |p_i||p_j|P_l(\cos\theta_{i,j}) \tag{4.4}$$

with the momenta $p_{i,j}$, the angle $\theta_{i,j}$ between them and the Legendre Polynomials P_l.

Hereafter, additional selections are applied to two of these event shape quantities. The cosine of the angle θ_{BY} in CMS between the momentum of the reconstructed B_{sig} and the momentum of a nominal B meson is required to be between $-3 < \cos\theta_{BY} < 2$. This value should lie somewhere between -1 and 1, if the event was correctly reconstructed, such that only one massless particle is missing. Therefore this is a loose selection of expected B_{sig} candidates with only one missing neutrino. Lastly, the event-based ratio of the 2-nd to the 0-th order of the Fox Wolfram moments $R_2 = H_2/H_0$ are set to be less than 0.5 to reduce continuum, which is further described in section 5.1.

4.4.2 Tag B Reconstruction with Rest-of-Event

To reconstruct the B_{tag}, the hierarchical Full Event Interpretation (FEI) algorithm is used, which first reconstructs low-level particles like kaons and pions, then intermediate particles and finally B mesons. In every stage the most-likely particle candidates are selected and used for the next stage. For each B meson candidate the FEI provides a signal probability that quantifies the likelihood of a correctly reconstructed decay chain. [32]

All particles that are not associated to the given reconstructed candidates are defined to be Rest of Event (ROE). This ROE is build for both the B_{sig} and B_{tag} candidates to further build a Continuum Suppression (CS). To ensure a well-defined ROE, a simple mask is applied to select high quality tracks and calorimeter cluster. The mask criteria are shown in the table A.2 in the appendix. Charged tracks are required to have a transverse momentum greater than 0.1 GeV, to lie within CDC acceptance and to originate from the vicinity of the IP. Specifically, the transverse distance with respect to the IP needs to be smaller than 2 cm, while the point of closest approach to the IP must be less than 4 cm. ROE particle clusters in the ECL are also required to lie within CDC acceptance, as well as having energies greater than 0.1 GeV.

The hadronically reconstructed B_{tag} candidates are also undergoing some additional selections from the FEI, which are aligned with the calibration. The beam-constrained mass is defined as

$$M_{bc} = \sqrt{E_{\text{beam}}^2 - \mathbf{p}_B^2}, \tag{4.5}$$

with the beam energy E_{beam} and the four-momentum of the B_{tag}, and is required to be greater or equal to 5.272 GeV. This selection proves to be the most impactful, reducing the background efficiency from ≈ 0.728 to ≈ 0.159, while maintaining a signal efficiency of ≈ 0.747 in all data sets. The difference between the energy of the B_{tag} and half the CMS energy

$$\Delta E = \frac{E_{cms}}{2} - E_B \tag{4.6}$$

needs to lie within the window $(-0.15 \leq \Delta E \leq 0.1)$ GeV. The cosine of the angle between the thrust axis of the B_{tag} and thrust axis of ROE particles $\cos\theta_{\text{TBTO}}$ needs to be smaller or equal to 0.9, which helps suppress continuum and will be further discussed in section 5.1. As mentioned before, the FEI provides a signal probability for each reconstructed B_{tag} candidate that is required to be greater than 0.001. This loose selection does not discard any events and therefore does not influence the data sets, but will be used for calculating FEI systematics in section 6.3. At last, a Best Candidate Selection (BCS) is applied, where the candidates of each event are sorted by the signal probability and only the candidate with the highest value will be kept. This selection reduces the multiplicity of the events to 1 since for every event only one candidate is selected, changing the candidate-based data set to an event-based data set.

4.4.3 $\Upsilon(4S)$ Reconstruction

The selected B_{tag} candidate is finally combined with the signal-side B_{sig} candidates to form an $\Upsilon(4S)$ candidate. Another ROE including the mask with selection criteria shown in table A.2 is constructed, including all detected particles that are not associated with either B meson. A final selection is applied on the $\Upsilon(4S)$ candidates, demanding less than 2 charged ROE particles.

4.5 Resulting Event Distributions

Applying all the selection criteria shown in table A.3 and A.4 enhances the signal events over the background. Looking at the tables, one can see that for each data set the background got reduced to less than 0.3 % of the raw data set, while 17.22 %, 18.18 % and 19.07 % of the signal events maintain in the complete data set, electron and muon channel, respectively. This can also be seen in the graphs A.1-A.6 in the appendix. It shows the distributions of the different variables, on which selections were employed, in the same order how they were applied to the specified data sets. Each graph builds on the preceding ones, showing the respective distribution with all selections applied from the graphs before, which demonstrates the process of enhancing the signal events over the background.

In semileptonic decays, the neutrino escapes detection since it interacts only via the weak interaction. Its presence therefore has to be inferred indirectly from the missing energy and momentum of the event. Since the tag-side B meson was reconstructed in only hadronic final states, the four-momenta from all particles in the event are known except for the neutrino on the signal-side. This allows the missing mass squared to be calculated as the difference between the known initial four-momentum of the e^+e^- collision $\mathbf{p}_{e^+e^-}$ and the reconstructed four-momenta of all visible final state particles $\mathbf{p}_i$:

$$M_{\text{miss}}^2 = (\mathbf{p}_{e^+e^-} - \Sigma_i \mathbf{p}_i)^2. \tag{4.7}$$

If the signal event was correctly reconstructed, the calculated M_{miss}^2 is expected to peak around the neutrino mass squared, which would be approximately zero. Detector resolution, imperfect reconstruction and residual background processes broaden this peak and may produce entries at positive or negative values. Background events containing additional missing particles or incorrectly reconstructed final states typically exhibit much broader distributions. Consequently, the missing mass squared provides excellent discrimantion between signal and background and is therefore chosen as the fitting variable in the maximum-likelihood fit in section 6.2.

The missing mass squared distributions of the reconstructed B_{sig} meson, after the mentioned selections were applied, are depicted in figure 4.2(a) for the complete data set and figures 4.2(b) and 4.2(c) for the electron and muon channel. Looking at the histograms, the expected clear peak of the signal events

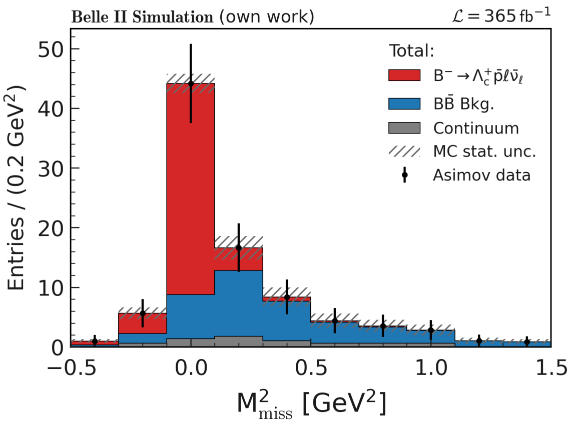

(a) Missing mass squared in the complete data set.

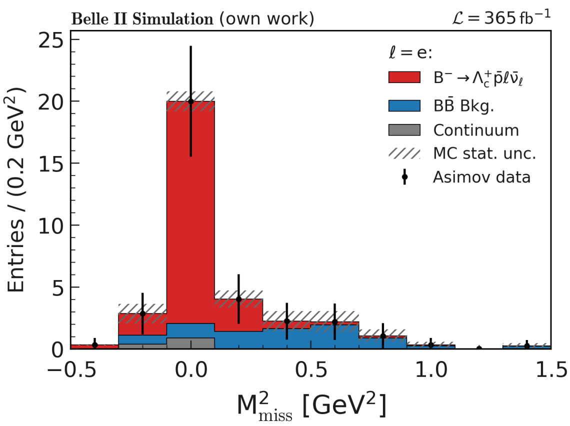

(b) Missing mass squared in the electron channel.

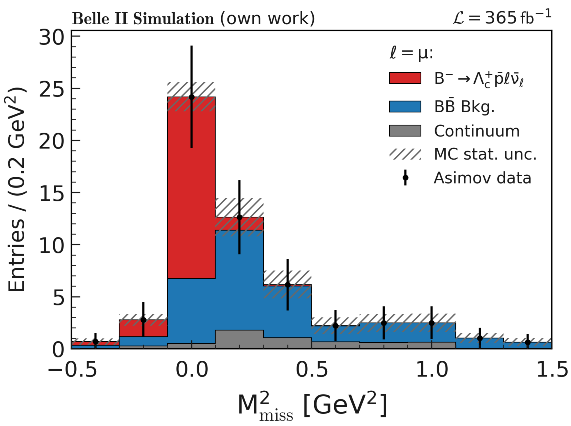

(c) Missing mass squared in the muon channel.

Figure 4.2: Distributions of the calculated missing mass squared of the reconstructed B_{sig} meson in the complete data set and the electron or muon channel. The red bars are the signal MC events, in blue are the $B\bar{B}$ background channels and in grey the continuum events. Asimov data was used and its uncertainty is shown, as well as the MC statistical uncertainties.

appears for every data set at $M_{\text{miss}}^2 \approx 0$. However, by comparing the electron and muon channel one can see that the $B\bar{B}$ background is more pronounced in the muon channel than in the electron channel. This difference is primarily caused by the PID performance of the Belle II detector. As described in section 3.2, muons are identified in the KLM subdetector based on their penetration through the detector material. Charged pions with sufficiently high momentum may produce a similar detector signature and are therefore more likely to be misidentified as muons. This increases to the overall $B\bar{B}$ background contribution in the muon channel, leading to the larger background observed in the M_{miss}^2 distribution. In contrast, electron identification exploits the characteristic electromagnetic shower in the ECL together with tracking information, resulting in a significantly lower hadron misidentification probability.

In addition, the continuum contribution is found to be very small, especially in the electron channel where several bins contain no continuum events. The limited statistics of the continuum templates can lead to numerical instabilities in the template fit which will be further investigated in section **??**.

CHAPTER 5

Background Analysis

Despite the clean experimental environment provided by the Belle II detector, several background events can mimic the signal topology of the decay $B^- \to \Lambda_c^+ \bar{p} \ell^- \bar{\nu}_\ell$. The dominant contributions originate from continuum production and generic $B\bar{B}$ decays, while smaller contributions arise from incorrectly reconstructed signal candidates. The following sections describe the background composition and the investigation of a veto of specific decays to improve the signal purity.

5.1 Continuum Suppression

The largest non-$B\bar{B}$ background at the $\Upsilon(4S)$ resonance originates from continuum production,

$$e^+e^- \to q\bar{q}, \qquad q = u, d, s, c.$$

Unlike $B\bar{B}$ events, which are produced nearly at rest in the CMS and therefore have a rather spherical event topology and smaller momentum, continuum events are dominated by two back-to-back jets resulting from the high momentum and fragmentation of the outgoing quarks. Based on these topological differences, which can also be seen in figure 5.1, continuum background can be effectively suppressed.

As mentioned before in section 4.4.1, the event-shape observable of the Fox Wolfram R_2 moment is required to be less than 0.5, which excludes jet-like events with $R_2 \approx 1$. Furthermore, the biggest impact on suppressing the continuum has the selection criterion of $\cos\theta_{\mathrm{TBTO}} \leq 0.9$, which was already mentioned in section 4.4.2. This cosine of the angle between the thrust axis of the reconstructed B_{tag} candidates and the thrust axis of the ROE tends to be small for signal events, whereas continuum events are strongly peaked near 1, also due to their jet-like topology. In figures A.2(a), A.4(a) and A.6(a) of the appendix the selection on the $\cos\theta_{\mathrm{TBTO}}$ is shown for the complete data set, as well as for the electron and muon channel, after the selections on $\cos\theta_{BY}$, Fox Wolfram R_2, M_{bc} and ΔE were already applied.

This simple selection removes a large fraction of the remaining continuum background while maintaining a high signal efficiency, which can also be seen in the cutflow tables A.3 and A.4. Since the continuum contribution after all reconstruction steps is comparatively small, more sophisticated multivariate continuum suppression techniques were not required.

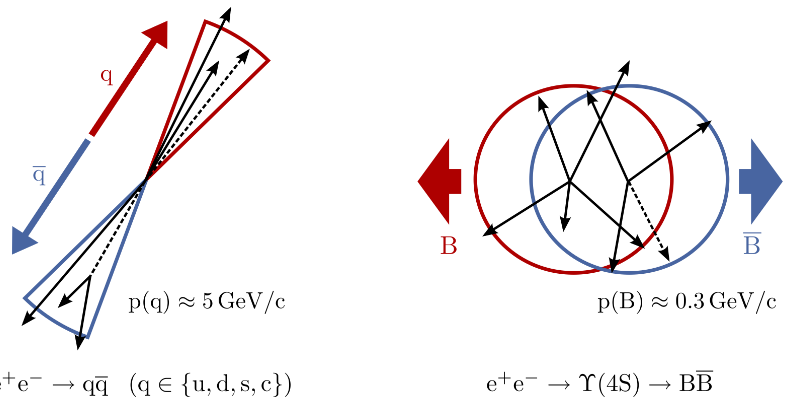

Figure 5.1: The topology of continuum and $B\bar{B}$ events at Belle II are depicted. The quarks of continuum events have high momenta and possess a jet-like structure, while $B\bar{B}$ events have low momentum and thus a spherical shape.[32]

5.2 Background Composition

After the event reconstruction and selection, the remaining background is dominated by generic $B\bar{B}$ events. These mainly arise from semileptonic and hadronic B meson decays in which unrelated particles are incorrectly combined to form a signal candidate. Such combinatorial backgrounds often contain genuine Λ_c baryons or other charmed baryons and therefore exhibit kinematic properties similar to those of the signal.

Different decay channels of the remaining $B\bar{B}$ background are depicted in the pie chart in figure 5.2. The 10 most common $B\bar{B}$ decay channels are highlighted in different shades of blue, which make up a total of almost 50 % of all the $B\bar{B}$ background events. A different decay channel with a Λ_c than the wanted signal decay is the most common $B\bar{B}$ decay channel with about 11.11 %, surviving all the aforementioned selection criteria from section 4.4. Besides that, many B mesons first decay into a Σ_c^{++}, Σ_c^{+} or Σ_c^{*+}, which later decays into a Λ_c and a pion. Because of the large contribution of these decays in the remaining $B\bar{B}$ background, a veto was constructed to reject events that form a Σ_c and later decay into Λ_c. This could greatly reduce background especially in the muon channel, since the $B\bar{B}$ contribution is still quite large compared to the electron channel, which was mentioned before in section 4.5.

5.3 Investigation of a Σ_c Veto

To further decrease $B\bar{B}$ background, decays involving a Σ_c can be vetoed, meaning even if these events pass all previously applied selection criteria, they will be rejected if the specified particles are present in the reconstructed event. As mentioned before, for the decay of $B^- \to \Lambda_c^+ \bar{p} \ell^- \bar{\nu}_\ell$ most $B\bar{B}$ background events inhabit a Σ_c^{++}, Σ_c^{+} or Σ_c^{*+} that further decay into

$$\Sigma_c^{++} \to \Lambda_c^+ \pi^+, \qquad \Sigma_c^{+} \to \Lambda_c^+ \pi^0 \quad \text{and} \quad \Sigma_c^{*+} \to \Lambda_c^+ \pi^0.$$

For each Σ_c, dedicated background MC samples were created, which contain one million generated events of the decays into the respective Σ_c that are shown in the pie chart in figure 5.2. As for the signal

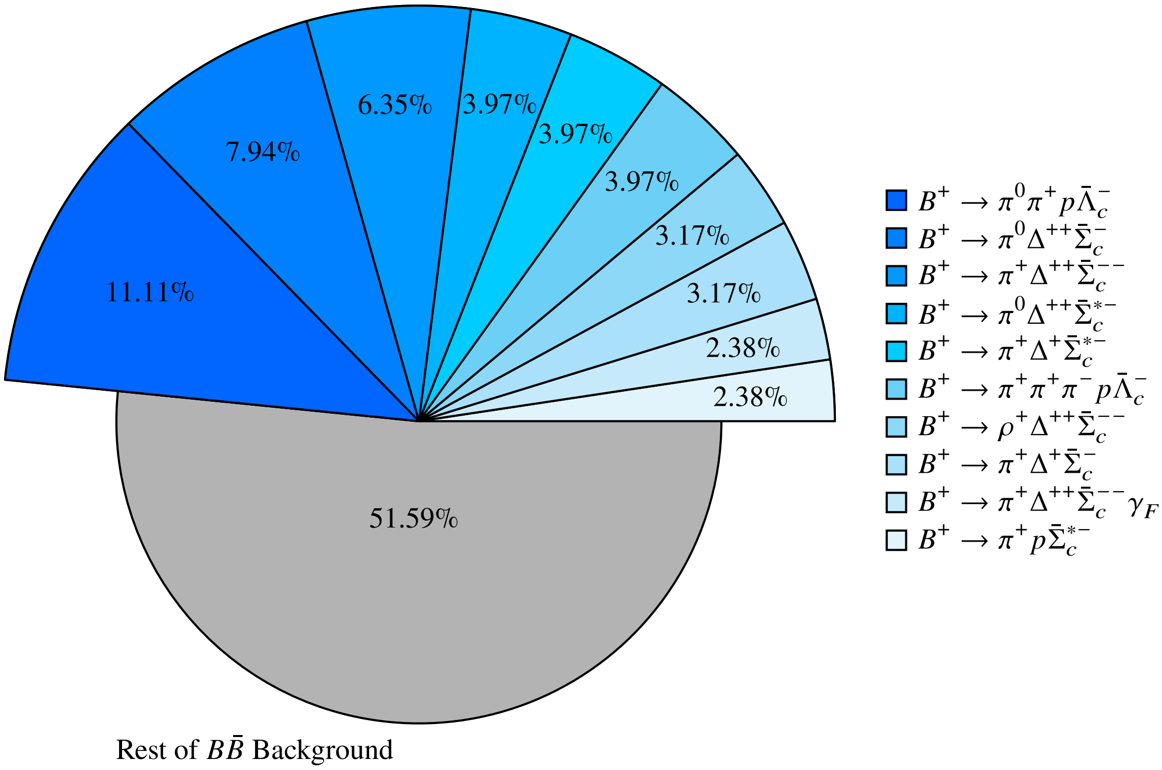

Figure 5.2: The composition of the $B\bar{B}$ background is shown. Highlighted are the 10 most common decay channels, which make almost 50 % of the total generic $B\bar{B}$ background events.

MC sample described in section 4.1, the PHSP decay model was also used to generate these dedicated Σ_c background MC samples. Subsequently, a veto window will be defined around the mass of the investigated Σ_c baryon and events within this window will be discarded. This construction of the veto is demonstrated in detail for the Σ_c^{++} since the process is analog for the other Σ_c baryons.

5.3.1 Validation of the Σ_c^{++} veto

First the Σ_c^{++} veto was investigated since it decays into a charged pion instead of a neutral pion, making the reconstruction easier. For the validation process, a dedicated background sample containing one million events of the decay chain

$$B^- \to \left(\Sigma_c^{++} \to (\Lambda_c^+ \to pK^-\pi^+)\pi^+\right)\bar{\Delta}^{--}\pi^- \tag{5.1}$$

was used. In these samples Σ_c^{++} candidates are formed by combining Λ_c^+ candidates, which were reconstructed the same way as in the signal events mentioned in section 4.4.1, with charged pions. In addition, the Λ_c candidates were combined with electrons and muons for the case that electrons or muons got misidentified as pions. The pions, electrons and muons are required to be “good tracks”, defined in section 4.4.1, and the mass of the reconstructed Σ_c^{++} candidates needs to be between $(2.1 < M_{\Sigma_c^{++}} < 2.6)$ GeV. This results in mass distributions of the Σ_c^{++} candidates shown in the figure

5.3. The blue entries show all reconstructed candidates while the grey entries are falsely reconstructed Σ_c^{++} candidates. One can see rising entry numbers of falsely reconstructed Σ_c^{++} with higher mass. This originates from wrong combinations of the particles from the decay chain for reconstructing the Σ_c^{++}, where more possibilities for combining arise at higher masses thanks to an increased available phase space. Looking at the graph 5.3(a) for the decay into $\Lambda_c^+\pi^+$, the red outline depicts correctly reconstructed decays which form a narrow peak at the mass of the Σ_c baryon: $M_{\Sigma_c^{++}} = 2453.97 \pm 0.14\,\text{MeV}$ [35]. The wrong combinations of the decay also show a smaller peak at the same mass value, indicating a relation to the correct reconstructions. This is caused by the pions of the $\Sigma_c^{++} \to \Lambda_c^+\pi^+$ and $\Lambda_c^+\pi^+$ decays being interchangable, resulting in the same decay chain. The "Truth-Matching" algorithm was used to determine the correct reconstructed candidates, which checks the identity of each particle and also the identity of their mother particle. When the two pions are exchanged, their PDG number does not change since they are the same particle type, but the PDG number of their mother particles are different, classifying this as a false reconstruction.

The distributions of the $\Lambda_c^+e^+$ and $\Lambda_c^+\mu^+$ combinations are shown in graph 5.3(b) and 5.3(c) respectively. As expected there are less candidates overall present in the histograms and no Σ_c^{++} was correctly reconstructed since the Σ_c^{++} only decays into $\Lambda_c^+\pi^+$. Nevertheless, a smaller peak still appears over the combinatorial background, which is more pronounced in the muon than in the electron channel. This also reflects the higher misidentification rate between muons and pions which also causes the higher $B\bar{B}$ background contribution in the muon channel, discussed in section 4.5. These peaks appear at smaller masses than for the reconstruction with the π^+, at $\approx 2.425\,\text{GeV}$ for the reconstruction with e^+ and $\approx 2.445\,\text{GeV}$ for the reconstruction with μ^+. Since the lepton mass is smaller than the pion mass, the calculated invariant mass is systematically shifted to lower values. The shift is larger for electrons than for muons because of the electron mass being smaller.

Because clear peaks were visible in the dedicated Σ_c^{++} background sample, the veto will now be applied to the data sets that are used in the rest of the analysis.

5.3.2 Application of the Σ_c^{++} Veto

After validating the veto it is now applied to the MC data that is used to search for the $B^- \to \Lambda_c^+\bar{p}\ell\bar{\nu}_\ell$ decays at Belle II. First the invariant mass of the Σ_c^{++} candidates reconstructed via $\Lambda_c^+\pi^+$, $\Lambda_c^+e^+$ and $\Lambda_c^+\mu^+$ are shown for the $B\bar{B}$ background sample in figures 5.4 like in the validation. In the reconstruction with e^+ and μ^+ in the graphs 5.4(b) and 5.4(c) only the combinatorial background can be seen with no visible peak at the mass values from the validation. Merely in the histogram 5.4(a) of the reconstruction with π^+ appears a small elevation of the entries at the Σ_c^{++} mass, thus only for this distribution the veto will be tested.

To apply the veto all events from the data sets will be discarded if they have at least one Σ_c^{++} candidate within a defined veto mass window, shown in the aforementioned graphs by the yellow dashed lines. To evaluate the veto, the significance Z, defined as

$$Z = \frac{S}{\sqrt{S+B}}, \tag{5.2}$$

with S being the number of signal and B the number of background events, is calculated in the missing mass squared graphs 4.2. The resulting significance values for applied veto windows of different widths around the Σ_c^{++} mass can be seen in table 5.1. With the assumed branching fraction

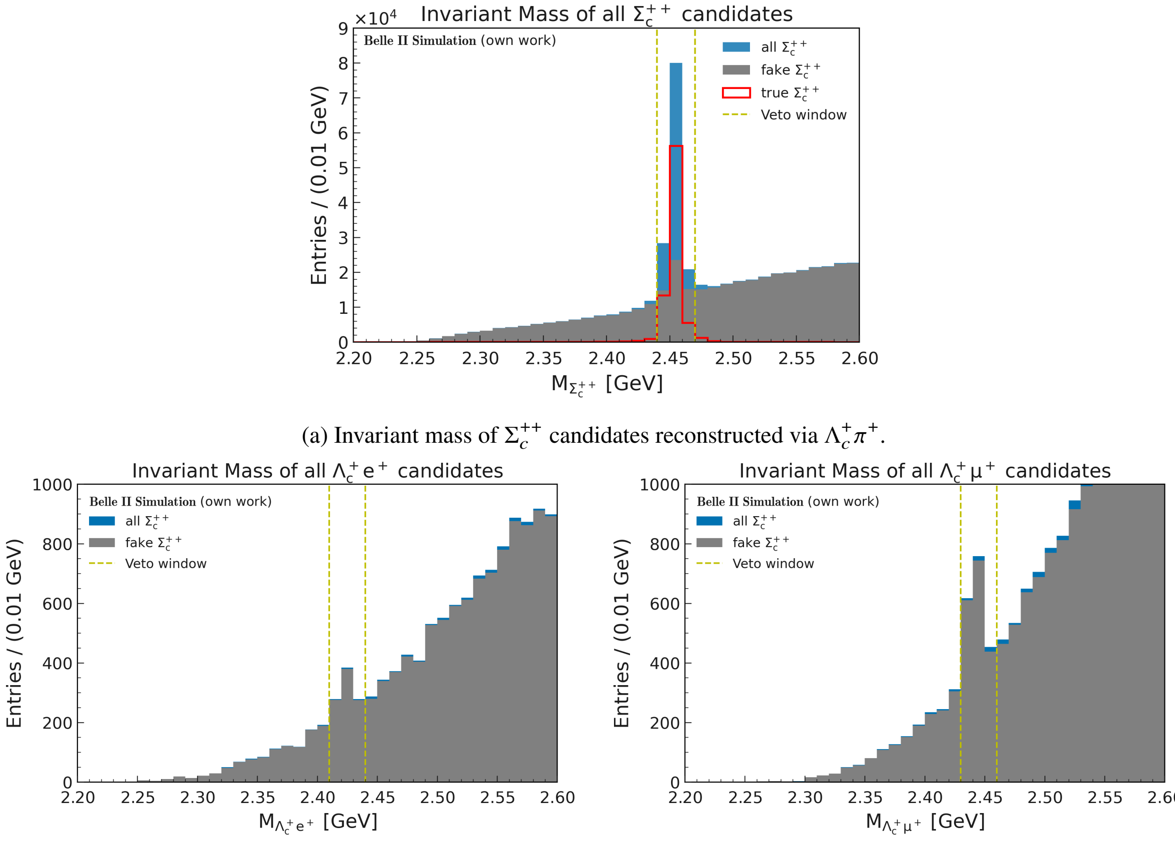

(a) Invariant mass of Σ_c^{++} candidates reconstructed via $\Lambda_c^+\pi^+$.

(b) Invariant mass of Σ_c^{++} candidates reconstructed via $\Lambda_c^+ e^+$. (c) Invariant mass of Σ_c^{++} candidates reconstructed via $\Lambda_c^+\mu^+$.

Figure 5.3: Distribution of the invariant mass of Σ_c^{++} candidates reconstructed via $\Lambda_c^+\pi^+$, $\Lambda_c^+ e^+$ and $\Lambda_c^+\mu^+$ respectively from dedicated background samples. The blue entries show all candidates, the red outline shows events that were correctly reconstructed and in grey are the falsely reconstructed Σ_c^{++} candidates. The yellow lines indicate the mass window, in which events will be discarded.

$\mathcal{B}_{\text{assumed}}(B^- \to \Lambda_c^+ \bar{p}\ell\bar{\nu}_\ell) = 2.5 \times 10^{-5}$, the significance without the veto is $Z_{\text{total}} = 4.7357\,\sigma$ for the complete data set, $Z_e = 4.1076\,\sigma$ for the electron channel and $Z_\mu = 2.8068\,\sigma$ for the muon channel. The highest significance can be obtained for the combined data set, although the $B\bar{B}$ background is smaller in the electron channel. Because of the discussed higher $B\bar{B}$ background distribution the significance of the muon channel is the lowest, being under $3\,\sigma$. If the events are now discarded when at least one Σ_c^{++} candidate is inside a veto window of just 6 MeV width, the significance drops to values of $Z_{\text{total}} = 3.5807\,\sigma$, $Z_e = 3.1029\,\sigma$ and $Z_\mu = 2.1190\,\sigma$. For every data set the significance decreased by $\approx 1.15\,\sigma$, $\approx 1.00\,\sigma$ and $\approx 0.62\,\sigma$, affecting the data sets with originally higher significance more than the ones which had a smaller significance. Applying the veto window presented in the graphs 5.3 and 5.4 with a width of 30 MeV give the significances $Z_{\text{total}} = 1.9197\,\sigma$, $Z_e = 1.6878\,\sigma$ and $Z_\mu = 1.1320\,\sigma$, reducing these values by almost 60 %. This shows that enlarging the veto window leads to a continuous reduction of the significance and the highest significance is achieved by not applying any veto.

The distributions shown in figure 5.4 explain this behaviour since no distinct Σ_c^{++} peak can be observed in the $B\bar{B}$ background, not like in the dedicated Σ_c^{++} background sample. Instead, the invariant mass

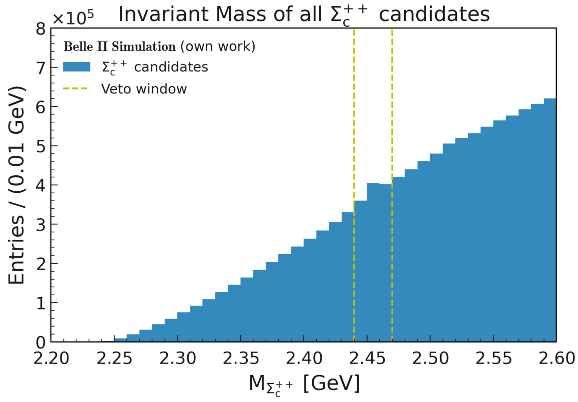

(a) Invariant mass of Σ_c^{++} candidates reconstructed via $\Lambda_c^+\pi^+$.

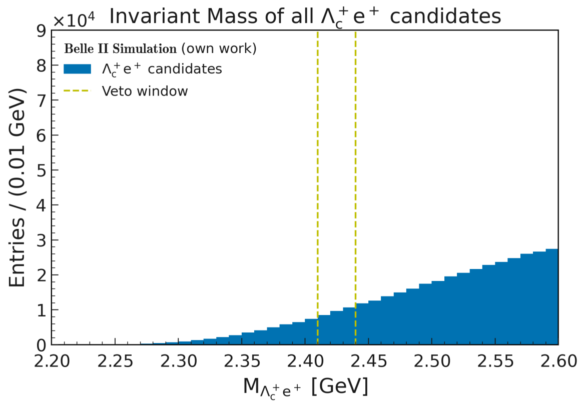

(b) Invariant mass of Σ_c^{++} candidates reconstructed via $\Lambda_c^+e^+$.

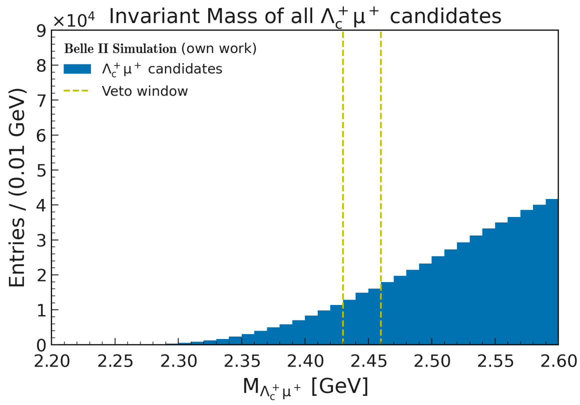

(c) Invariant mass of Σ_c^{++} candidates reconstructed via $\Lambda_c^+\mu^+$.

Figure 5.4: Distribution of the invariant mass of Σ_c^{++} candidates, reconstructed via $\Lambda_c^+\pi^+$, $\Lambda_c^+e^+$ and $\Lambda_c^+\mu^+$ respectively at generic $B\bar{B}$ background samples. The blue entries show all candidates reconstructed as a Σ_c^{++}. Here only for the decay with the π^+ a small peak in the region of the Σ_c^{++} mass is visible, in the others no peak is visible. The yellow lines indicate the veto window, in which events will be discarded.

distributions are dominated by a large combinatorial background that increases over the considered mass range. Consequently, a substantial fraction of background events falls into the veto window purely due to random combinations of reconstructed particles rather than genuine Σ_c^{++} decays. At the same time, signal events are removed whenever such accidental candidates are reconstructed in the event. As a result, the veto reduces the signal efficiency more strongly than it suppresses the relevant background, leading to a decrease of the significance. Therefore, no Σ_c^{++} veto is applied in the remainder of this analysis.

Although the investigated Σ_c^{++} veto does not improve the expected sensitivity of the present analysis, several possible refinements could be explored in future studies. The dominant limitation is the large combinatorial background arising from multiple $\Lambda_c^+\pi^+$ combinations per event. A possible approach would be to introduce a BCS, retaining only the most likely Σ_c^{++} candidate according to a suitable quality criterion. Furthermore, additional selection requirements on the quality of the reconstructed candidates or a dedicated kinematic fit could improve the mass resolution and reduce random combinations. Such optimizations would require careful validation to ensure that they do not introduce biases into the signal

Veto cut	**Significance**		
	Total	Electron	Muon
No veto	4.7357	4.1076	2.8068
$(2.452 < M < 2.458)$ GeV	3.5807	3.1029	2.1190
$(2.45 < M < 2.46)$ GeV	3.0777	2.6721	1.8213
$(2.445 < M < 2.465)$ GeV	2.4154	2.1377	1.4109
$(2.44 < M < 2.47)$ GeV	1.9197	1.6878	1.1320

Table 5.1: Significance after applying the veto with different widths of the invariant mass window on the Σ_c^{++} candidates. One can see that the significance decreases with the width of the veto window. The highest significance occurs when no veto is applied.

selection.

5.3.3 Potential Veto for Σ_c^+ and Σ_c^{*+}

A validation of the Σ_c^+ and Σ_c^{*+} was performed analogously to the Σ_c^{++} study. Dedicated background samples were generated including the two dominant $B\bar{B}$ decay channels containing these intermediate Σ_c states. The Λ_c^+ is required to decay into the same final state as used in the signal events as in equation 4.2 and in the veto for the Σ_c^{++} in equation 5.1. The remaining decay chains in the dedicated Σ_c background samples are defined as:

$$B^- \to (\bar{\Sigma}_c^- \to \bar{\Lambda}_c^- \pi^0)\Delta^{++}\pi^0, \qquad B^- \to (\bar{\Sigma}_c^{*-} \to \bar{\Lambda}_c^- \pi^0)\Delta^{++}\pi^0,$$
$$B^- \to (\bar{\Sigma}_c^{*-} \to \bar{\Lambda}_c^- \pi^0)\Delta^{+}\pi^+, \qquad B^- \to (\bar{\Sigma}_c^{*-} \to \bar{\Lambda}_c^- \pi^0)\Delta^{+}\pi^+.$$

The veto construction follows the same principle as for the Σ_c^{++}, however the Λ_c^+ candidates are combined with π^0 candidates. Since the pion here is neutral, it cannot be directly detected in the Belle II detector and thus has to be reconstructed from two photons, where the mass of the pion is required to fulfill $(0.08 < M_{\pi^0} < 0.20)$ GeV. The resulting invariant mass distributions of the Σ_c^+ and Σ_c^{*+} candidates can be seen in figures 5.5. Both cases show a dominant combinatorial background with only a small fraction of correctly reconstructed Σ_c baryons, which still peaks at the mass of the respective Σ_c mass $M_{\Sigma_c^+} = 2452.65^{+0.22}_{-0.16}$ MeV and $M_{\Sigma_c^{*+}} = 2517.4^{+0.7}_{-0.5}$ MeV [35]. In contrast to the Σ_c^{++} veto in graph 5.3(a), the correctly reconstructed candidates do not form a narrow peak over the combinatorics. This is mainly caused by the additional reconstruction of the neutral pion, which introduces a large number of possible photon pair combinations. Multiple photons can originate from other particles. For example the $\Delta^+ \to p\pi^0$ decay also produces a pi^0 which further decays into photons, creating higher combinatorics and thus a large fraction of incorrectly reconstructed π^0 candidates. This effect is further amplified by the relatively poor energy resolution of low-energy photons in the ECL, which leads to a broadening of the reconstructed π^0 mass and, consequently, a smearing of the reconstructed Σ_c invariant mass [30]. As a result, the signal-to-background ratio for Σ_c^+ and Σ_c^{*+} reconstruction is significantly worse than in the charged pion case.

Furthermore, “Truth-Matching” confirms this behaviour, as a substantial fraction of reconstructed candidates cannot be uniquely matched to a true Σ_c decay. This arises from ambiguous photon assignments in the π^0 reconstruction and from cases where one or both photons do not originate from the same true parent particle. Consequently, the reconstructed candidate either fails to be assigned a valid

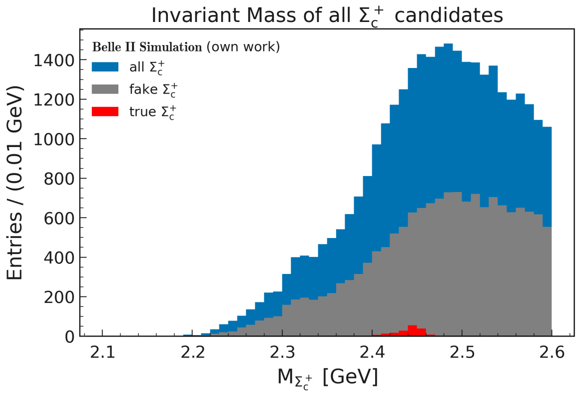

(a) Invariant mass of Σ_c^+ candidates reconstructed via $\Lambda_c^+\pi^0$.

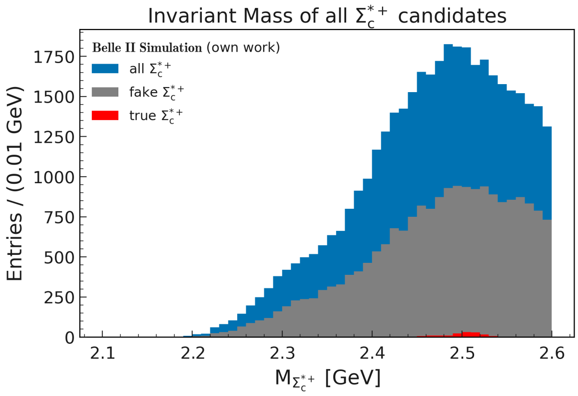

(b) Invariant mass of Σ_c^{*+} candidates reconstructed via $\Lambda_c^+\pi^0$.

Figure 5.5: Distribution of the invariant mass of Σ_c^+ and Σ_c^{*+} candidates, both reconstructed via $\Lambda_c^+\pi^0$ from dedicated background samples. The blue entries show all candidates, the red outline shows events that were correctly reconstructed and in grey are the falsely reconstructed Σ_c candidates.

mother particle or is incorrectly matched, leading to fake Σ_c candidates for a large fraction of entries.

Due to the absence of a clearly identifiable Σ_c peak and the lack of improvement in the expected significance for the Σ_c^{++} in any data set, these vetoes were not further investigated in the analysis.

CHAPTER 6

Signal Extraction

After applying all selection criteria, the sensitivity of the analysis is evaluated by extracting the expected signal contribution from the simulated event distributions. Since this study is based entirely on MC simulation and Asimov data sets, the following procedure determines the expected performance of the analysis rather than measuring the branching fraction from experimental data.

The signal extraction is performed using a binned template fit to the missing mass squared distributions of the reconstructed B_{sig} mesons using the maximum likelihood method. Signal, $B\bar{B}$ background and continuum events are represented by templates, while systematic uncertainties affecting their normalization and shape are incorporated into the statistical model. The fitted signal strength is subsequently used to determine an upper limit on the branching fraction of the decay $B^- \to \Lambda_c^+ \bar{p} \ell^- \bar{\nu}_\ell$, for the complete data set as well as the electron and muon channels separately.

6.1 Maximum Likelihood Estimation

Maximum Likelihood Estimation (MLE) is a statistical method used to determine the values of model parameters that provide the best description of the observed data. Given a set of observations and a parametrized statistical model, a likelihood function is constructed that quantifies the probability of observing the measured data for a given choice of parameters. In most analyses of particle physics, the models of observable distribution is described by a Probability Density Function (PDF) $f(x_i; p, q)$. It is typically formulated in terms of a set of independent observables x_i and a parameter of interest (POI), denoted p. A set of nuisance parameters q modify the normalization and shape of the PDF and affect the relation between x_i and p. Such nuisance parameters can be for example resolution parameters or tracking efficiencies. For a set of independent observations x_i, the likelihood function is defined as the product of the PDF evaluated at each observed event,

$$\mathcal{L}(\mu, \alpha) = \prod_i^N f(x_i; p, q), \tag{6.1}$$

where N is the total number of observed events. The likelihood provides a quantitive measure of how well a given choice of parameters describes the observed data set. [37]

In practice, high-energy physics analyses are often performed in a binned representation of the data. The observable space is divided into bins with the bin-center x_i, and is weighted by the observed number of events in that bin n_i:

$$\mathcal{L}(\mu, \alpha) = \prod_i^N f(x_i; p, q)^{n_i}.$$

The best estimate for the POI, the maximum likelihood estimator $\hat{p}$, is the value of p, where the likelihood function has its maximum. In an analysis with a large amount of observed events and a small number of observables, it might be efficient to instead minimize a binned negative log-likelihood, defined as

$$-\log \mathcal{L}(p, q) = -\sum_i^N n_i \cdot \log f(x_i; p, q). \tag{6.2}$$

Here, the computation time scales with the total amount of bins N rather than the number of events. This binned likelihood is less precise than the unbinned likelihood because the information of the exact position of the event in each bin is discarded, but with sufficiently small bin sizes this loss of precision becomes negligible. [37]

The observed events consist of signal S and background B contributions, both being encoded as templates with known shapes $f_S(x)$ and $f_B(x)$. The expected number of events in bin i is denoted as $m_i = pS_i(q) + B_i(q)$ with the POI p, which also acts as a signal strength modifier: $p = 1$ corresponds to the nominal signal prediction, while $p = 0$ describes the background-only hypothesis. With a Poisson probability of observing n_i events in a bin while expecting $m_i = pS_i(q) + B_i(q)$ events, the PDF including signal and background is:

$$\mathcal{P}(x|p, q) = \prod_i \text{Pois}(n_i | pS_i(q) + B_i(q)) \prod_{j=1}^{n_i} \frac{pS_i(q) f_S(x_{ij}) + B_i(q) f_B(x_{ij})}{pS_i(q) + B_i(q)}. \tag{6.3}$$

Nuisance parameters might be described by constraint terms $C_j(p_j)$, typically in the form of Gaussian or log-normal distributions. Assuming Poisson statistics for each bin, the full likelihood can be constructed as a product over multiple statistically independent regions or (decay) channels,

$$\mathcal{L}(p, q) = \prod_r \prod_i \text{Pois}(n_{r,i} | m_{r,i}(p, q)) \cdot \prod_j C_j(q_j), \tag{6.4}$$

where r indexes the different regions of the analysis. [37]

The statistical inference is performed using the profile likelihood method, in which the nuisance parameters are optimized (profiled) for each fixed value of p. This procedure yields the profile likelihood function, which is used for parameter estimation, hypothesis testing and the construction of confidence intervals. The statistical model, fit implementation and determination of an upper limit in this work are based on the HistFactory formalism and are performed using pyhf via the interface provided by cabinetry.

6.2 The Template Fit

To estimate the expected sensitivity of the analysis, a binned template fit is performed using the missing mass squared distribution M_{miss}^2 as the discriminating observable. The expected event distributions are represented by separate templates for the signal MC, $B\bar{B}$ background and continuum after multiple selections were applied, as it was shown in section 4.5. Their normalizations are described by the parameters of the statistical model, while systematic uncertainties are incorporated through nuisance parameters. The complete statistical model therefore consists of the POI p together with the nuisance parameters q, like it was described in the previous section 6.1.

Looking at the distributions in figures 4.2, little to no entries at a missing mass squared below -0.3 GeV^2 and above 0.5 GeV^2 can be seen. Before performing the template fit the binning of these histograms was optimized such that each bin contains a sufficient number of expected events. Thus two neighboring bins above and below the peak were combined to reduce the impact of statistical fluctuations originating from the finite size of the simulated samples. The signal peak around $M^2_{\mathrm{miss}} \approx 0$ was kept finely binned to preserve its discriminating power, while larger bins were used in low-statistics tails of the distribution. For the template fit the bins above 1.1 GeV^2 were additionally discarded since they did not hold sufficient entries after merging two bins. This leads to the rebinned missing mass squared distributions shown in figures 6.1, on which the template fit was performed. Since the continuum template contains only a very small number of events in any data set even after the rebinning procedure, its normalization cannot be reliably constrained by the fit, leading to large statistical fluctuations and an unstable fit. For this reason, the continuum normalization was fixed to its nominal expectation, while only the signal and $B\bar{B}$ background normalizations were treated as free parameters. The distributions of the complete data set, as well as the electron and muon channel will be fitted separately to analyse the effect of splitting the sample in the two channels and the differences between them.

The post-fit uncertainties obtained from the template fit are used to quantify the impact of the individual uncertainty sources on the expected signal sensitivity. These uncertainties are subsequently propagated to the statistical interpretation presented in the following sections, where an expected upper limit on the branching fraction of $B^- \to \Lambda_c^+ \bar{p} \ell^- \bar{\nu}_\ell$ is determined.

6.3 Systematic Uncertainties

Besides the statistical uncertainty originating from the finite size of the MC samples, additional systematic effects influence the expected event yields and therefore the sensitivity of the analysis. These uncertainties arise from imperfections in the detector simulation, residual differences between MC simulation and the experimental data, and uncertainties associated to the reconstruction and identification of particles. Deviations like this need to be accounted for with systematic corrections to achieve a more realistic and complete estimation.

The systematic uncertainties are incorporated into the statistical model using a book-keeping framework named **SysVar**. Based on the event weights obtained from the individual correction factors, SysVar constructs a covariance matrix describing the correlations between all channels, templates and histogram bins. This covariance matrix is diagonalized to determine its eigenvectors, which define a set of statistically independent variations. Each eigenvariation is then implemented in the template fit as a fully correlated nuisance parameter. All of these nuisance parameters modify the normalization of the affected templates or its shape according to its corresponding uncertainty and is constrained during the profile likelihood fit [38]. In this way, the fit propagates both statistical and systematic uncertainties consistently to the final statistical model. The systematic uncertainties considered in this analysis originate from the Full Event Interpretation calibration, the charged particle tracking efficiency and the particle identification efficiency.

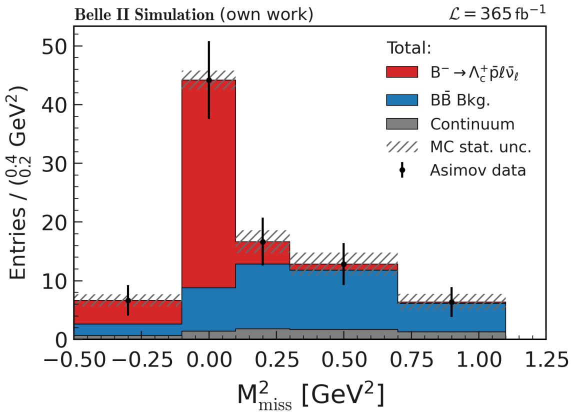

(a) Missing mass squared of the reconstructed B_{sig} meson in the complete data set.

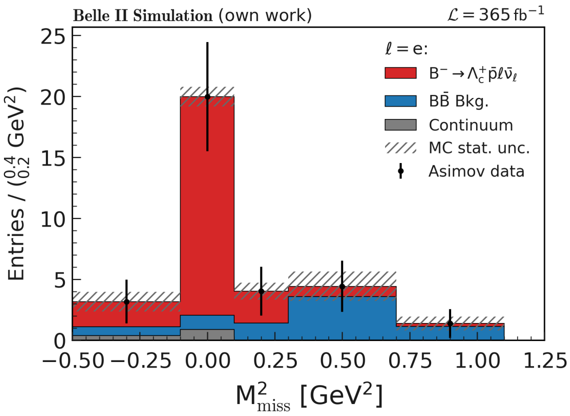

(b) Missing mass squared of the reconstructed B_{sig} meson in the electron channel.

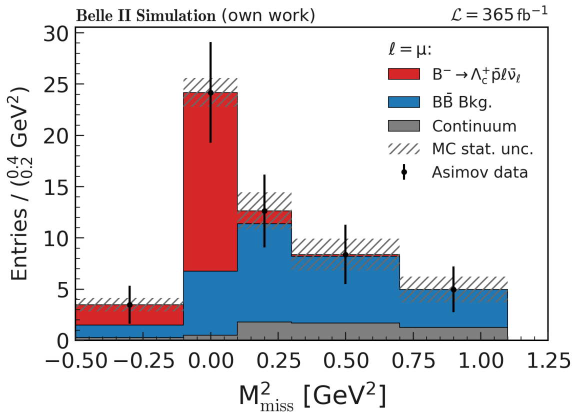

(c) Missing mass squared of the reconstructed B_{sig} meson in the muon channel.

Figure 6.1: Distributions of missing mass squared of the reconstructed B_{sig} meson in the complete data set, electron and muon channel respectively. The red bars are the signal MC events, in blue are the $B\bar{B}$ background channels and in grey the continuum events. Asimov data was used and its uncertainty is shown, as well as the MC statistical uncertainties.

6.3.1 Full Event Interpretation Corrections

The reconstruction of the tag-side B meson is performed using the Full Event Interpretation (FEI), which was already discussed in section 4.2. As mentioned in that section, only events fulfilling

$$\texttt{SignalProbability} > 0.001$$

are retained. For all selected candidates, calibration factors from the FEI are applied to correct residual differences between the simulated data and the reconstruction. The corresponding correction tables depend on the selected signal probability region and provide both nominal correction and its uncertainty. For every reconstructed B_{tag} candidate, an event weight is assigned according to the corresponding calibration factor from the correction table. The uncertainty of this correction reflects the limited precision of the calibration procedure and propagates directly to the expected event yields.

6.3.2 Track Efficiency

The reconstruction efficiency of charged particles is another important source of systematic uncertainty. Since the signal decay shown in equation 4.2 contains five reconstructed charged tracks, the corresponding tracking efficiency correction is determined from the total number of reconstructed tracks in the event. Belle II provides correction factors together with their uncertainties for different track multiplicities. These corrections account for residual differences in the charged particle reconstruction efficiency between MC simulation and collision data.

6.3.3 Particle Identification Efficiency

The identification of charged particles is based on information from several Belle II subdetectors. To ensure high purity lepton selection, the requirements

$$\texttt{electronID} > 0.9 \quad \text{and} \quad \texttt{muonID} > 0.9$$

are applied for electons and muon, which were mentioned before in section 4.4.1. Because these tight PID requirements are imposed only on the signal lepton, PID corrections are required only for the electron and muon candidates in the signal reconstruction. In addition to the lepton identification efficiencies, the corresponding pion and kaon misidentification rates are included, for the case that the pion or kaon got falsey identified as the considered lepton. The associated calibration factors and uncertainties are obtained from dedicated Belle II control samples.

6.4 Impact of the Uncertainties

Since this analysis is based exclusively on simulated events, the fit is conducted on an Asimov data set, which was constructed from the nominal signal and background expectations. Consequently, the maximum likelihood fit returns the nominal values for the normalization parameters, corresponding to a signal strength, which is the POI, of $p = 1$. The purpose of the fit is therefore not to extract the signal yield, but to determine the expected statistical and systematic uncertainties by profiling the nuisance parameters. To quantify the contribution of the individual uncertainty sources, the fit is repeated while successively enabling the different groups of nuisance parameters. The resulting overall uncertainty can be expressed as

$$\sigma_{\text{overall}} = \sqrt{\sigma_{\text{stat}}^2 + \sigma_{\text{MC}}^2 + \sigma_{\text{FEI}}^2 + \sigma_{\text{track}}^2 + \sigma_{\text{PID}}^2},$$

where the individual terms denote the statistical uncertainty of the Asimov data set σ_{stat}, the finite MC statistics σ_{MC} and the systematic uncertainties originating from the FEI calibration σ_{FEI}, charged track reconstruction σ_{track} and PID σ_{PID}. The discussed uncertainties for the signal and generic $B\bar{B}$ background templates are summarized in table 6.1. Comparing the three fitted data sets, the combined fit provides

Uncertainty type	**Template Fit Uncertainties**					
	Signal			Background		
	Total	Electron	Muon	Total	Electron	Muon
Stat. only	±0.19404	±0.25212	±0.31070	±0.24303	±0.57948	±0.27449
MC stat.	±0.09798	±0.12723	±0.30959	±0.12265	±0.29053	±0.27373
FEI syst.	±0.02479	±0.02689	±0.02284	±0.03140	±0.02200	±0.03416
track syst.	±0.00395	±0.00405	±0.00359	±0.00468	±0.00378	±0.00466
PID syst.	±0.00139	±0.00152	±0.00096	±0.00277	±0.00428	±0.00228
Overall unc.	±0.21881	±0.28368	±0.43922	±0.27408	±0.64861	±0.38918

Table 6.1: Impact of the different uncertainties on the signal and background template obtained from the combined template fit, as well as the electron and the muon channel template fit. The first row shows the statistical uncertainty without systematic nuisance parameters applied. The remaining rows list the individual systematic contributions, while the last row describes the overall uncertainty obtained when all uncertainty sources are included simultaneously.

the smallest overall uncertainty with around ±0.219 and ±0.275 with regard to the nominal yield of 1 for the signal and background template, respectively. This is due to its much larger effective event sample. For the signal template, the electron channel achieves with ±0.284 a better precision than the muon channel with ±0.440, whereas the latter exhibits the larger uncertainty because of its substantially higher generic $B\bar{B}$ background, which reduces the statistical sensitivity of the fit. Analogously, the background template shows a lower uncertainty in the muon channel than in the electron channel because of the higher $B\bar{B}$ background. This results in the background normalization being statistically better constrained, leading to a smaller relative uncertainty.

Additionally, the statistical uncertainty appears to be the dominant contribution in all considered data sets. Looking at the signal template, only considering the Asimov data statistical uncertainty already contributes around 89 % for the complete data set and electron channel and 70 % for the muon channel to the overall uncertainty. This is expected, as the available signal and background samples contain only a limited number of reconstructed events after the event selections described in section 4.5. The second-largest contribution originates from the MC statistics, which becomes particularly important in the muon channel because of its larger background contribution and the consequently smaller signal purity. In contrast, the systematic uncertainties associated with the FEI calibration, tracking efficiency and particle identification are considerably smaller. Among these, the FEI corrections represents the largest contribution, whereas the uncertainties related to the tracking efficiency and PID remain below the one percent level with respect to the nominal signal yield. This demonstrates that the sensitivity of the analysis is currently limited primarily by statistical effects rather than detector-related systematic uncertainties. The dominant statistical contribution originates from the relatively small number of events remaining after the complete reconstruction and selection procedure. In addition, the investigated decay is expected to have a very small branching fraction, resulting in only a limited number of reconstructed signal candidates even in the simulated samples. Consequently, the statistical precision represents the main limitation of the present analysis.

6.5 Determination of the Upper Limit

The statistical model described in the previous sections is finally used to determine an expected upper limit on the branching fraction of the decay

$$B^- \to \Lambda_c^+ \bar{p} \ell^- \bar{\nu}_\ell.$$

Since no recorded Belle II data are considered in this study, the upper limit is derived from a background-only Asimov data set using the profile-likelihood method. In contrast to the template fit discussed in the previous sections, where a signal-plus-background Asimov data set is used to determine the expected parameter uncertainties, the POI is fixed to $p = 0$ for the background-only hypothesis. Therefore, obtained limits represent the expected sensitivity of this analysis in the absence of a signal. All statistical and systematic uncertainties discussed in the previous sections are incorporated into the statistical model as nuisance parameters q in the likelihood fit.

The upper limits are determined using the CL_S method. According to that, the profile-likelihood test statistic is evaluated for different values of the signal strength parameter μ_{CL_S}, and the corresponding CL_S values are calculated. The resulting CL_S scans for the complete data set as well as for the individual electron and muon channels are shown in figure A.7 in the appendix. In it, the green and yellow bands indicate the expected $\pm 1\sigma$ and $\pm 2\sigma$ variations around the median expected limit under the background-only hypothesis. The observed CL_S curves are identical to the median expected curves since these upper limits were obtained from Asimov data sets. The intersection with the horizontal line at $CL_S = 0.1$ determines the quoted expected upper limits at 90 % confidence level in the following. [39]

For the combined fit of the electron and muon channels, an expected upper limit of is obtained at a

$$\boxed{\mathcal{B}(B^- \to \Lambda_c^+ \bar{p} \ell^- \bar{\nu}_\ell) < 4.3 \times 10^{-6} \quad (90\,\%\ \text{CL})}$$

confidence level of 90 %. As expected, the combined fit provides the strongest constraint on the branching fraction by exploiting the statistical power of both decay channels simultaneously. The electron channel alone yields a more stringent upper limit than the muon channel

$$\boxed{\mathcal{B}(B^- \to \Lambda_c^+ \bar{p} e^- \bar{\nu}_e) < 5.2 \times 10^{-6} \quad (90\,\%\ \text{CL})}$$

$$\boxed{\mathcal{B}(B^- \to \Lambda_c^+ \bar{p} \mu^- \bar{\nu}_\mu) < 9.4 \times 10^{-6} \quad (90\,\%\ \text{CL}),}$$

which is consistent with the larger generic $B\bar{B}$ background observed in the muon channel. The increased background level reduces the statistical sensitivity of the fit and therefore results in a weaker upper limit.

Overall, the obtained upper limits demonstrate that the sensitivity of the analysis is primarily determined by the available event statistics. While detector-related systematic uncertainties have only a minor impact on the final result, the limited number of reconstructed signal candidates and the remaining background events dominate the expected sensitivity. Future analyses based on larger Belle II data samples are therefore expected to further tighten the achievable upper limit or enable a direct measurement of the branching fraction. In addition, the sensitivity could be further improved by increasing the signal reconstruction efficiency, for example through the inclusion of additional Λ_c^+ decay modes, the combination of hadronic and semileptonic tagging methods or further optimization of the event selection and background suppression.

CHAPTER 7

Conclusion

In this analysis, a search for the baryonic semileptonic decay

$$B^- \to \Lambda_c^+ \bar{p} \ell \bar{\nu}_\ell, \quad \ell = e, \mu$$

was performed using simulated Belle II data and the hadronic tagging method. Since the neutrino cannot be detected, the reconstruction of the signal B meson relies on the full reconstruction of the tag-side B meson via the Full Event Interpretation, allowing the missing four-momentum of the signal-side decay to be determined. The missing mass squared was used as the final discriminating variable for estimating the impact of individual uncertainties and calculating an expected upper limit of the branching fraction of this decay.

An event selection was developed to suppress continuum and generic $B\bar{B}$ backgrounds while retaining a large fraction of the dedicated signal event sample. The applied selections significantly reduced the background contributions down to less than 0.3 % compared to the raw data, leading to a clear signal peak around $M^2_{\text{miss}} \approx 0$ in the simulated signal sample. For the full data set 17.22 % of the signal events maintain after the selections, for the electron and muon channel 18.18 % and 19.07 % of the signal events retain, respectively. The remaining background was found to be dominated by $B\bar{B}$ decays, with a noticeably larger contribution in the muon channel than in the electron channel, mostly originating from pions being misidentified as muons. This difference resulted in a reduced statistical sensitivity of the muon channel throughout this analysis.

Several additional background rejection strategies were investigated in an attempt to further decrease the $B\bar{B}$ background. In particular, vetoes against intermediate Σ_c states were developed and validated using dedicated simulated background samples. Although the Σ_c^{++} veto successfully identified most of the correctly reconstructed resonance candidates, it also removed a substantial fraction of signal events because of the large combinatorial background present in generic $B\bar{B}$ events. Consequently, the highest statistical significance was obtained by not applying any veto and the significance only decreased for all investigated veto window sizes. Analogous studies for Σ_c^+ and Σ_c^{*+} showed even stronger combinatorial backgrounds already for the dedicated background samples, mainly caused by the reconstruction of neutral pions from photon pairs. Since none of the investigated vetoes improved the expected sensitivity, they were not included in the final event selection.

The signal extraction was performed using a binned template fit. The fit incorporated statistical uncertainties together with systematic uncertainties originating from the Full Event Interpretation calibration, tracking efficiencies and particle identification corrections. As the study was based exclusively on simulated samples, an Asimov data set was used, such that the fit served to evaluate the expected uncertainties rather than extract a physical signal yield. The results showed that the overall uncertainty is dominated by the statistical component, while detector-related systematic uncertainties contribute only to a comparatively small fraction. This demonstrates that the current sensitivity of the analysis is primarily limited by the available event statistics after the full selection.

Finally, a 90 % confidence level upper limit on the branching fraction of the investigated decay was determined. The combined electron and muon channels provide the strongest expected constraint,

$$\mathcal{B}(B^- \to \Lambda_c^+ \bar{p} \ell^- \bar{\nu}_\ell) < 4.3 \times 10^{-6},$$

while the individual electron and muon channels yield upper limits of $\mathcal{B}(B^- \to \Lambda_c^+ \bar{p} e^- \bar{\nu}_e) < 5.2 \times 10^{-6}$ and $\mathcal{B}(B^- \to \Lambda_c^+ \bar{p} \mu^- \bar{\nu}_\mu) < 9.4 \times 10^{-6}$, respectively. The better sensitivity of the combined fit reflects the larger effective event sample, whereas the weaker constraint in the muon channel originates from its higher $B\bar{B}$ background.

Although no signal extraction from experimental Belle II data was performed within this work, the developed reconstruction, background studies and statistical framework provide a solid basis for future analyses. The present study demonstrates that the analysis is feasible and establishes the expected sensitivity under the current assumptions. Future improvements could focus on increasing the available signal statistics by including additional Λ_c^+ decay modes or combining of hadronic and semileptonic tagging techniques. Furthermore, more sophisticated approaches to suppress combinatorial backgrounds, for example through optimized candidate selection, may further improve the signal sensitivity.

As Belle II continues to accumulate significantly larger integrated luminosities, the statistical limitations observed in this work are expected to decrease, improving the sensitivity to the decay $B^- \to \Lambda_c^+ \bar{p} \ell \bar{\nu}_\ell$ at Belle II. An eventual observation and measurement of its branching fraction would provide an important contribution to the understanding of semileptonic baryonic B meson decays and help reduce the remaining semileptonic gap. A more complete description of the inclusive semileptonic decay rate improves the determination of the CKM matrix element $|V_{cb}|$, one of the key parameters of the Standard Model of Particle Physics. Therefore, this analysis represents an important step towards future measurements of semileptonic baryonic B meson decays at Belle II, contributing to a more complete understanding of semileptonic B decays and enabling increasingly precise consistency tests of the Standard Model of Particle Physics.

APPENDIX A

Additional Tables and Graphs

A.1 Event Selection

Event selection		
B_{sig} meson		**B_{tag} meson**
$e^{\pm}$ goodTrack $p_{e^{\pm}} > 0.3$ eID > 0.9	$\mu^{\pm}$ goodTrack $p_{\mu^{\pm}} > 0.3$ μID > 0.9	$M_{bc} \geq 5.272$ $-0.15 \leq \Delta E \leq 0.1$ $\cos\theta_{TBTO} \leq 0.9$
$2.1 < M_{\Lambda_c} < 2.5$		SignalProbability > 0.001
B_{sig} treeFit (conf_level = 0.001)		
$-3 < \cos\theta_{BY} < 2$ foxWolframR2 < 0.5		BCS with highest SignalProbability
$\Upsilon(4S)$ resonance		
$n^{ROE}_{charged} < 2$		

Table A.1: Summary of event selection criteria. "goodTrack" refers to $\theta \in$ CDC acceptance, $dr < 1.0$ cm, and $|dz| < 3.0$ cm. All mass and momentum selections are given in GeV.

ROE Selection	
track	**cluster**
$\theta \in$ CDC Acceptance $p_t > 0.1$ $\|dz\| < 4.0$ $dr < 2.0$	$\theta \in$ CDC Acceptance $E > 0.1$

Table A.2: Cuts of the simple ROE mask, which is applied to ensure well-defined B_{tag} candidates. All energy and momentum selections are given in GeV, all distance selections are in cm.

A.2 Cutflow Tables

Selection criteria	Complete data set			
	n_{events}	Mult.	Signal eff.	Bkg. eff.
Baseline	56823	2.750	1.0000	1.0000
$-3 < \cos\theta_{BY} < 2$	47034	2.702	0.9965	0.7538
Fox Wolfram $R_2 < 0.5$	45546	2.721	0.9930	0.7286
$M_{bc} \geq 5.272$	17360	2.711	0.7467	0.1572
$-0.15 \leq \Delta E \leq 0.10$	15803	2.438	0.6100	0.1290
$\cos\theta_{\text{TBTO}} \leq 0.9$	12939	2.444	0.5325	0.0957
SignalProbability > 0.001	12939	2.444	0.5325	0.0957
Highest SignalProbability	12939	1.000	0.2031	0.0439
$n_{\text{charged}}^{\text{ROE}} < 2$	9759	1.000	0.1875	0.0220
$2.28 < M_{\Lambda_c} < 2.295$	6887	1.000	0.1722	0.0027

Table A.3: Cutflow table of every selection that was applied to the data, for the complete data set. Depicted are the number of events, the multplicity, signal and background efficiency of every selection criteria. All mass and energy selections are given in GeV.

Selection criteria	Electron channel				Muon channel			
	n_{events}	Mult.	Signal eff.	Bkg. eff.	n_{events}	Mult.	Signal eff.	Bkg. eff.
Baseline	22754	2.638	1.0000	1.0000	38241	2.517	1.0000	1.0000
$-3 < \cos\theta_{BY} < 2$	18850	2.649	0.9937	0.7493	31571	2.443	0.9996	0.7562
Fox Wolfram $R_2 < 0.5$	18324	2.671	0.9908	0.7257	30538	2.456	0.9954	0.7300
$M_{bc} \geq 5.272$	8204	2.630	0.7430	0.1633	10519	2.423	0.7509	0.1541
$-0.15 \leq \Delta E \leq 0.10$	7502	2.354	0.6087	0.1333	9471	2.203	0.6115	0.1268
$\cos\theta_{\text{TBTO}} \leq 0.9$	6307	2.371	0.5347	0.1030	7529	2.215	0.5301	0.0920
SignalProbability > 0.001	6307	2.371	0.5347	0.1030	7529	2.215	0.5301	0.0920
Highest SignalProbability	6307	1.000	0.2163	0.0482	7529	1.000	0.2240	0.0450
$n_{\text{charged}}^{\text{ROE}} < 2$	5115	1.000	0.1982	0.0274	5384	1.000	0.2076	0.0214
$2.28 < M_{\Lambda_c} < 2.295$	3807	1.000	0.1818	0.0029	3626	1.000	0.1907	0.0028

Table A.4: Cutflow table of every selection that was applied to the data, for electron and muon channel separately. Depicted are the number of events, the multplicity, signal and background efficiency of every selection criteria. All mass and eneryg selections are given in GeV.

A.3 Selection Criteria for Complete Data Set

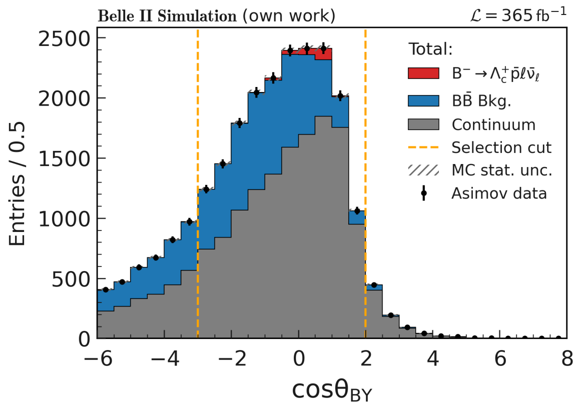

(a) The cosine of the angle θ_{BY} in CMS between the momentum of the reconstructed B_{sig} and the momentum of a nominal B meson.

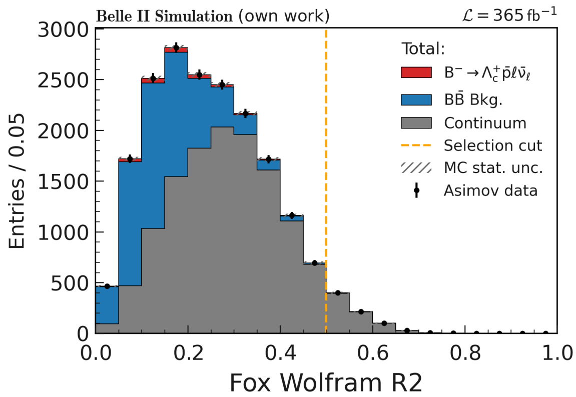

(b) Fox Wolfram moment R_2 of the reconstructed B_{sig} meson.

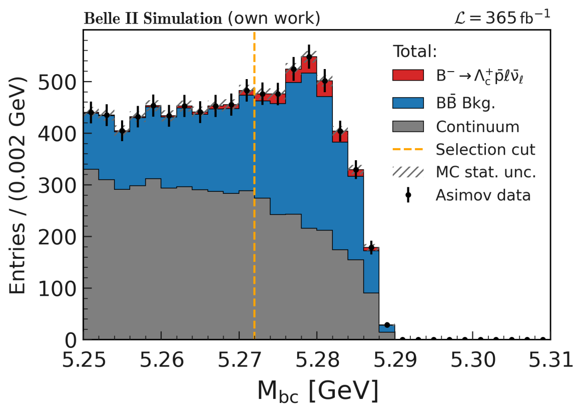

(c) Beam constrained mass of the B_{tag} meson.

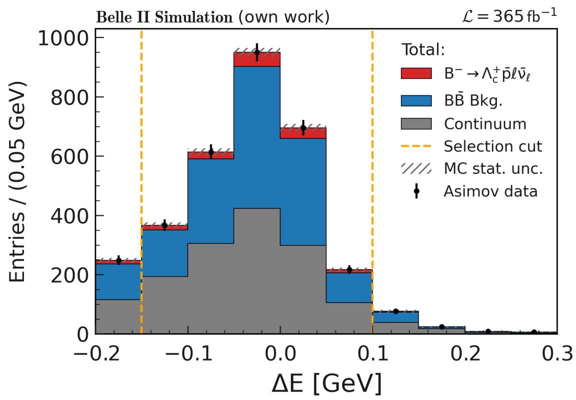

(d) The difference between the energy of the B_{tag} and half of the CMS energy.

Figure A.1: Distributions of the first four variables with their respective selections, depicted as orange dashed lines, on the complete data set. The order of the histograms corresponds to the order of the applied selection criteria. Each graph builds onto each other, showing the respective distribution with all selections applied from the graphs before on the same data set, demonstrating the process of enhancing the signal events over the background. The red bars are the signal MC events, in blue are the $B\bar{B}$ background channels and in grey the continuum events. Asimov data was used and its uncertainty is shown, as well as the MC statistical uncertainties.

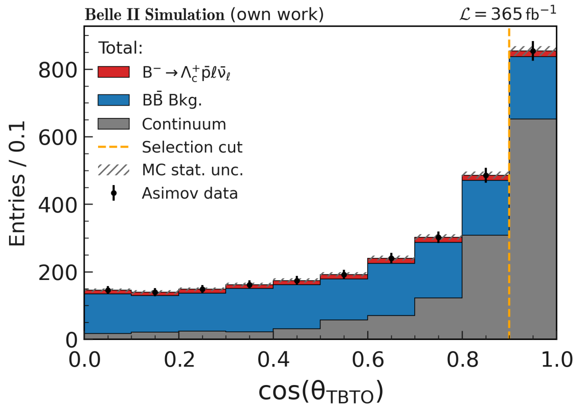

(a) The cosine of the angle between the thrust axis of the B_{tag} meson and the thrust axis of the ROE.

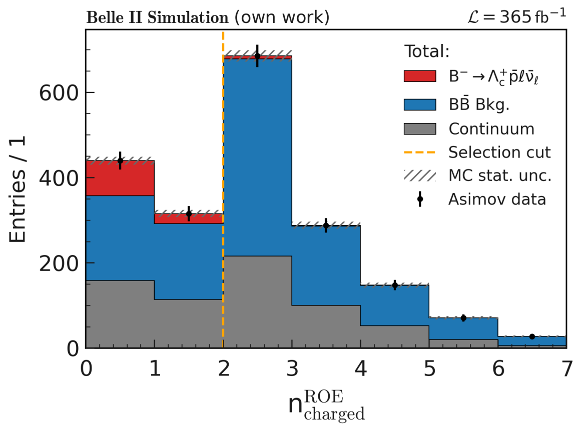

(b) Number of charged ROE particles of the $\Upsilon(4S)$ candidates.

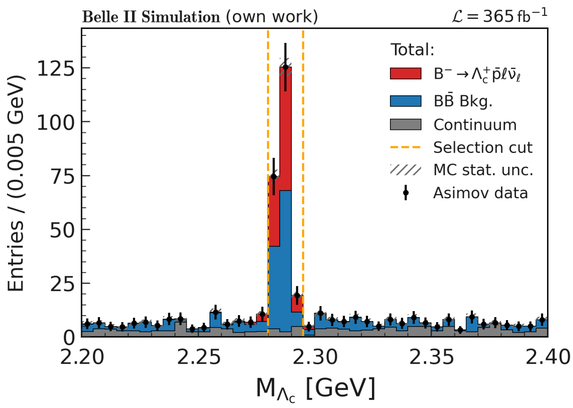

(c) Invariant mass of the reconstructed Λ_c candidates.

Figure A.2: Distributions of the last three variables with their respective selections, depicted as orange dashed lines, on the complete data set. The order of the histograms corresponds to the order of the applied selection criteria. Each graph builds onto each other, showing the respective distribution with all selections applied from the graphs before on the same data set, demonstrating the process of enhancing the signal events over the background. The red bars are the signal MC events, in blue are the $B\bar{B}$ background channels and in grey the continuum events. Asimov data was used and its uncertainty is shown, as well as the MC statistical uncertainties.

A.4 Selection Criteria for Electron Channel

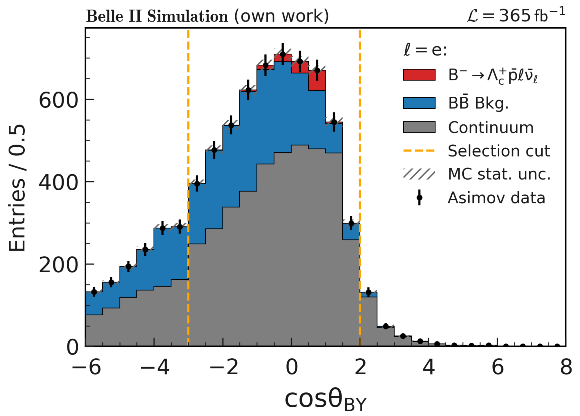

(a) The cosine of the angle θ_{BY} in CMS between the momentum of the reconstructed B_{sig} and the momentum of a nominal B meson.

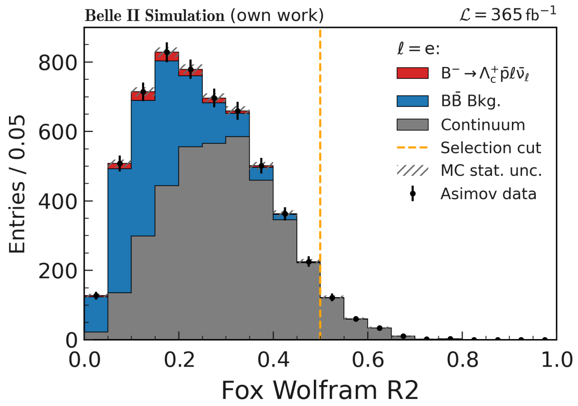

(b) Fox Wolfram moment R_2 of the reconstructed B_{sig} meson.

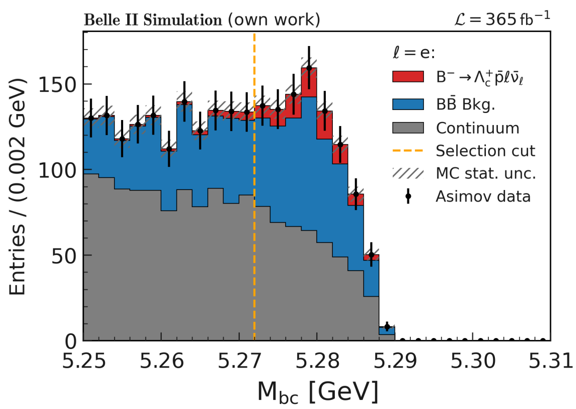

(c) Beam constrained mass of the B_{tag} meson.

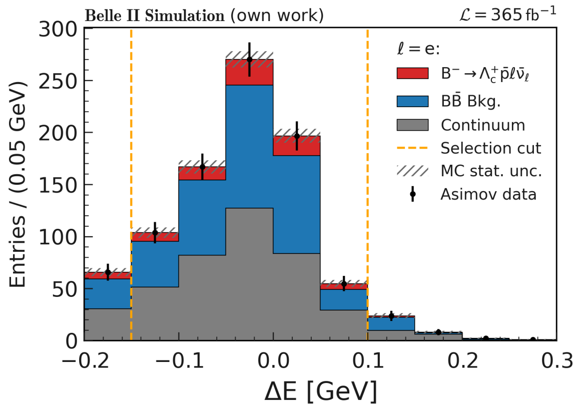

(d) The difference between the energy of the B_{tag} and half of the CMS energy.

Figure A.3: Distributions of the first four variables with their respective selections, depicted as orange dashed lines, in the electron channel. The order of the histograms corresponds to the order of the applied selection criteria. Each graph builds onto each other, showing the respective distribution with all selections applied from the graphs before on the same data set, demonstrating the process of enhancing the signal events over the background. The red bars are the signal MC events, in blue are the $B\bar{B}$ background channels and in grey the continuum events. Asimov data was used and its uncertainty is shown, as well as the MC statistical uncertainties.

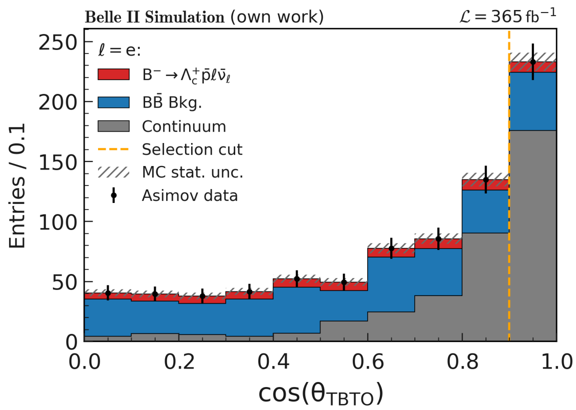

(a) The cosine of the angle between the thrust axis of the B_{tag} meson and the thrust axis of the ROE.

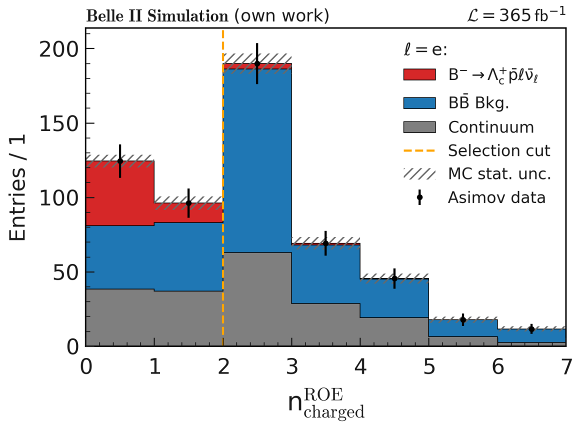

(b) Number of charged ROE particles of the $\Upsilon(4S)$ candidates.

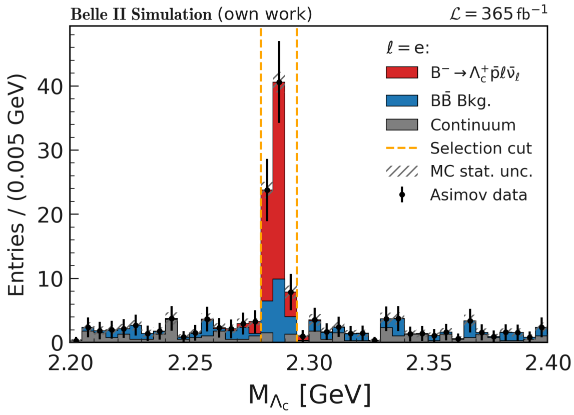

(c) Invariant mass of the reconstructed Λ_c candidates.

Figure A.4: Distributions of the last three variables with their respective selections, depicted as orange dashed lines, in the electron channel. The order of the histograms corresponds to the order of the applied selection criteria. Each graph builds onto each other, showing the respective distribution with all selections applied from the graphs before on the same data set, demonstrating the process of enhancing the signal events over the background. The red bars are the signal MC events, in blue are the $B\bar{B}$ background channels and in grey the continuum events. Asimov data was used and its uncertainty is shown, as well as the MC statistical uncertainties.

A.5 Selection Criteria for Muon Channel

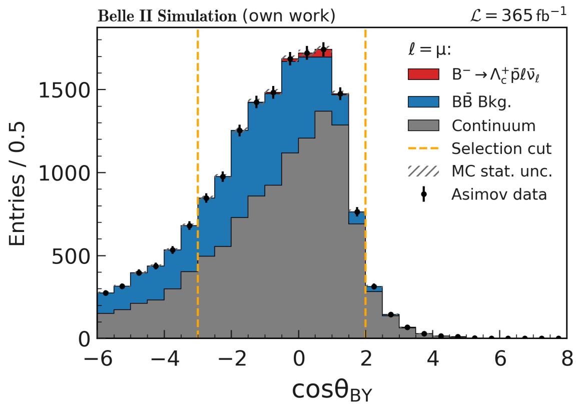

(a) The cosine of the angle θ_{BY} in CMS between the momentum of the reconstructed B_{sig} and the momentum of a nominal B meson.

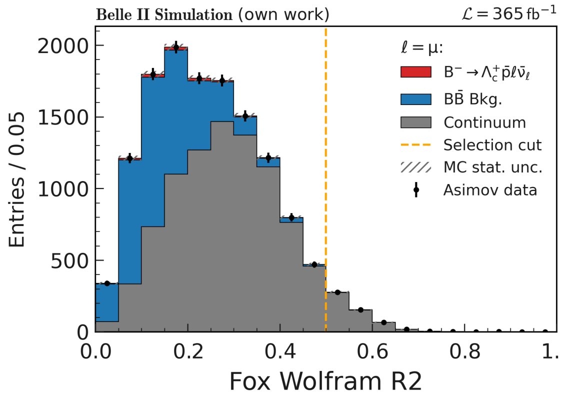

(b) Fox Wolfram moment R_2 of the reconstructed B_{sig} meson.

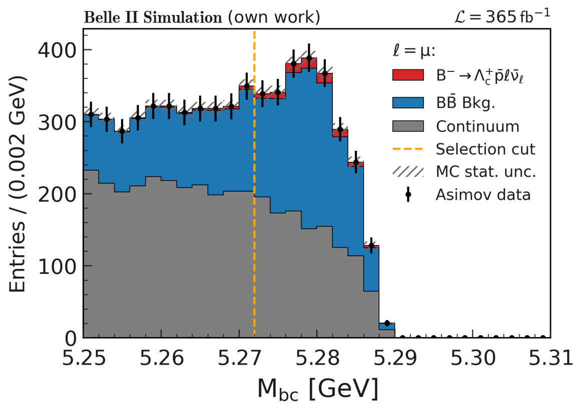

(c) Beam constrained mass of the B_{tag} meson.

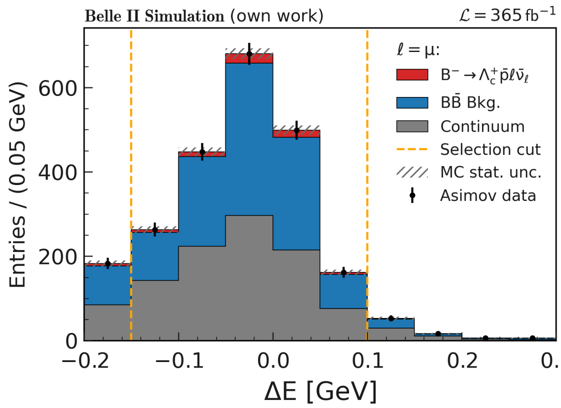

(d) The difference between the energy of the Btag and half of the CMS energy.

Figure A.5: Distributions of the first four variables with their respective selections, depicted as orange dashed lines, in the muon channel. The order of the histograms corresponds to the order of the applied selection criteria. Each graph builds onto each other, showing the respective distribution with all selections applied from the graphs before on the same data set, demonstrating the process of enhancing the signal events over the background. The red bars are the signal MC events, in blue are the $B\bar{B}$ background channels and in grey the continuum events. Asimov data was used and its uncertainty is shown, as well as the MC statistical uncertainties.

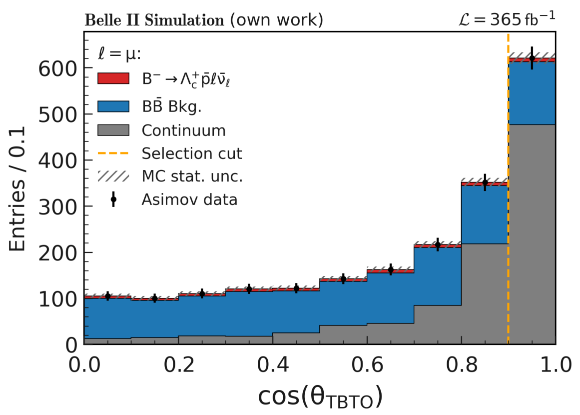

(a) The cosine of the angle between the thrust axis of the B_{tag} meson and the thrust axis of the ROE.

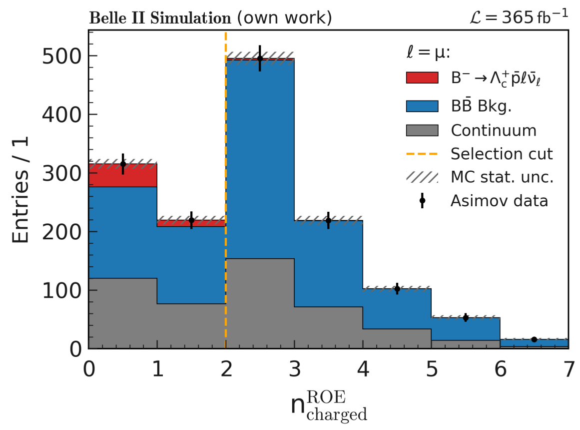

(b) Number of charged ROE particles of the $\Upsilon(4S)$ candidates.

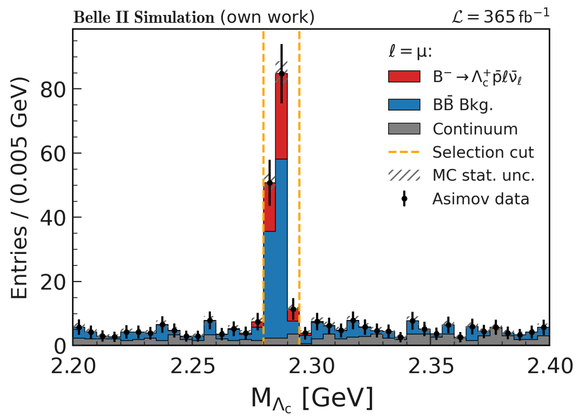

(c) Invariant mass of the reconstructed Λ_c candidates.

Figure A.6: Distributions of the last three variables with their respective selections, depicted as orange dashed lines, in the muon channel. The order of the histograms corresponds to the order of the applied selection criteria. Each graph builds onto each other, showing the respective distribution with all selections applied from the graphs before on the same data set, demonstrating the process of enhancing the signal events over the background. The red bars are the signal MC events, in blue are the $B\bar{B}$ background channels and in grey the continuum events. Asimov data was used and its uncertainty is shown, as well as the MC statistical uncertainties.

A.6 CL_S Curves

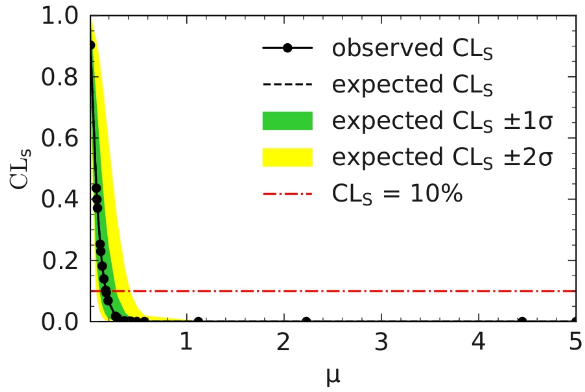

(a) CL_S curve in the complete data set.

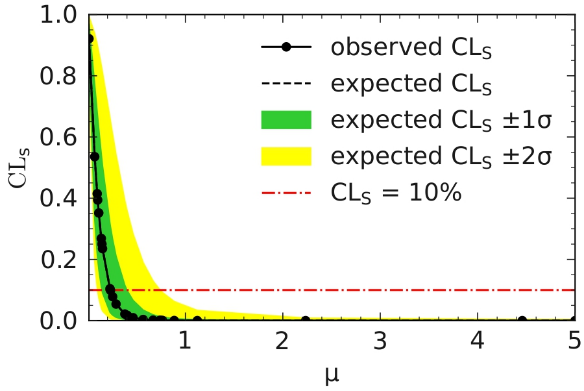

(b) CL_S curve in the electron channel.

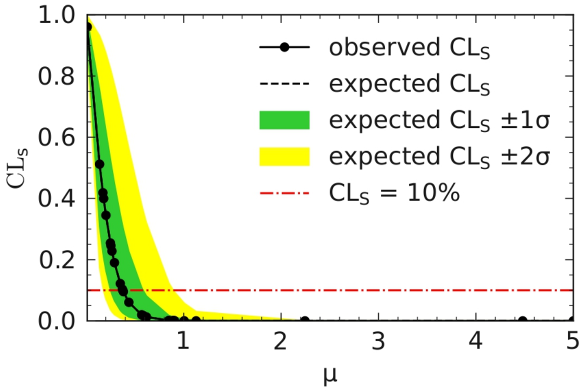

(c) CL_S curve in the muon channel.

Figure A.7: Expected and observed CL_S curves used to determine the 90 % confidence level upper limit for the complete data set, as well as the electron and muon channel seperately. The black dots and line show the observed CL_S, while the dashed line represents the median expected CL_S. The green and yellow bands indicate the $\pm 1\sigma$ and $\pm 2\sigma$ expected intervals. The red horizontal line corresponds to CL_S=0.1, whose intersection with the observed curve defines the quoted 90 % confidence level upper limit.

Bibliography

[1] A. Pich, *The Standard Model of Electroweak Interactions*, (2012) 52, arXiv: 1201.0537, URL: https://cds.cern.ch/record/1411131/?ln=de (cit. on p. 3).

[2] G. Gabrielse, S. E. Fayer, T. G. Myers and X. Fan, *Towards an Improved Test of the Standard Model's Most Precise Prediction*, 2019, arXiv: 1904.06174 [quant-ph], URL: https://arxiv.org/abs/1904.06174 (cit. on p. 3).

[3] L. C. ALEPH Collaboration DELPHI Collaboration, *Precision Electroweak Measurements on the Z Resonance*, Physics Reports **427** (2006) 257, ISSN: 0370-1573, URL: http://dx.doi.org/10.1016/j.physrep.2005.12.006 (cit. on p. 3).

[4] X. Fan, T. G. Myers, B. A. D. Sukra and G. Gabrielse, *Measurement of the Electron Magnetic Moment*, Phys. Rev. Lett. **130** (7 2023) 071801, URL: https://link.aps.org/doi/10.1103/PhysRevLett.130.071801 (cit. on p. 3).

[5] The ATLAS Collaboration, Aad G. et al, *Observation of a new particle in the search for the Standard Model Higgs boson with the ATLAS detector at the LHC*, Physics Letters B **716** (2012), ISSN: 0370-2693, URL: http://dx.doi.org/10.1016/j.physletb.2012.08.020 (cit. on p. 3).

[6] *Elementary Particle Physics*, URL: https://quantum.lassp.cornell.edu/lecture/elementary%5C_particle%5C_physics (visited on 24/04/2026) (cit. on p. 4).

[7] M. Thomson, *Modern Particle Physics*, Cambridge University Press, 2013, ISBN: 978-1-107-03426-6 (cit. on pp. 3, 5, 11, 18).

[8] L. Wolfenstein, *Parametrization of the Kobayashi-Maskawa Matrix*, Phys. Rev. Lett. **51** (21 1983) 1945, URL: https://link.aps.org/doi/10.1103/PhysRevLett.51.1945 (cit. on p. 5).

[9] Particle Data Group, Z. L. A. Ceccucci and Y. Sakai, *CKM Quark-Mixing Matrix*, (2026), URL: https://pdg.lbl.gov/2026/reviews/rpp2026-rev-ckm-matrix.pdf (cit. on pp. 5–7).

[10] C. Gross, A. Polosa, A. Strumia, A. Urbano and W. Xue, *Dark matter in the standard model?*, Physical Review D **98** (2018), ISSN: 2470-0029, URL: http://dx.doi.org/10.1103/PhysRevD.98.063005 (cit. on p. 7).

[11] F. R. KLINKHAMER, *NEUTRINO MASS AND THE STANDARD MODEL*, Modern Physics Letters A **28** (2013) 1350010, ISSN: 1793-6632, URL: `http://dx.doi.org/10.1142/S0217732313500107` (cit. on p. 7).

[12] M. Dine and A. Kusenko, *Origin of the matter-antimatter asymmetry*, Reviews of Modern Physics **76** (2003) 1, ISSN: 1539-0756, URL: `http://dx.doi.org/10.1103/RevModPhys.76.1` (cit. on p. 7).

[13] S. O. Bilson-Thompson, F. Markopoulou and L. Smolin, *Quantum gravity and the standard model*, Classical and Quantum Gravity **24** (2007) 3975, ISSN: 1361-6382, URL: `http://dx.doi.org/10.1088/0264-9381/24/16/002` (cit. on p. 7).

[14] Particle Data Group, A. El-Khadra and P. Urquijo, *Semileptonic b-Hadron Decays, Determination of V_{cb}, V_{ub}*, (2026), URL: `https://pdg.lbl.gov/2026/reviews/rpp2026-rev-vcb-vub.pdf` (cit. on p. 8).

[15] A. Ryd and D. e. a. Lange, *EvtGen: A Monte Carlo Generator for B-Physics*, (2005) (cit. on pp. 8, 16).

[16] Florian Herren, Raynette van Tonder, *Closing the knowledge gap in semileptonic $B \to X_c \ell \nu$ decays*, 2026, arXiv: `2605.03021` (cit. on p. 8).

[17] A. I. e. a. Belle II Collaboration, *Determination of $|V_{cb}|$ using $B \to D \ell \nu_\ell$ Decays at Belle II*, Phys. Rev. D **112** (2025), ISSN: 2470-0029, URL: `http://dx.doi.org/10.1103/vs8k-259v` (cit. on p. 8).

[18] C. Lyu, *Determination of $|V_{cb}|$ form factors of $\bar{B}^0 \to D^{*+} \ell^- \bar{\nu}_\ell$ decays with Belle II data*, Universität Bonn, 2024, URL: `https://hdl.handle.net/20.500.11811/11234` (cit. on p. 8).

[19] N. Rauls, *Measurement of the Branching Ratio $B \to D^{**} \ell \nu_\ell$ using the hadronic Full Event Interpretation with Belle II Data*, Universität Göttingen, 2024, URL: `https://dx.doi.org/10.53846/goediss-10602` (cit. on p. 8).

[20] S. Bifani, S. Descotes-Genon, A. R. Vidal and M.-H. Schune, *Review of lepton universality tests in B decays*, Journal of Physics G: Nuclear and Particle Physics **46** (2018) 023001, ISSN: 1361-6471, URL: `http://dx.doi.org/10.1088/1361-6471/aaf5de` (cit. on p. 9).

[21] CLEO Collaboration, G. Bonvicini et al, *Study of semileptonic decays of B mesons to charmed baryons*, Phys.Rev.D (1998) 9, arXiv: `9712008` (cit. on p. 9).

[22] BaBar Collaboration, J. P. Lees et al, *Search for $\bar{B} \to \Lambda_c^+ X \ell^- \bar{\nu}_\ell$ decays in events with a fully reconstructed B meson*, Phys.Rev.D **85** (2012) 7, URL: `https://link.aps.org/doi/10.1103/PhysRevD.85.011102` (cit. on p. 9).

[23] BaBar Collaboration, B. Aubert et al, *Evidence for B semileptonic decays into the charmed baryon Lambda_c+*, (2008) 16, arXiv: `0808.0011`, URL: `https://arxiv.org/abs/0808.0011` (cit. on p. 9).

[24] *SuperKEKB*,
URL: https://www.belle2.org/about%5C_us/superkekb%5C_accelerator/ (visited on 08/07/2026) (cit. on pp. 10, 11).

[25] R. W. G. Barr R. Devenish, *Particle Physics in the LHC era*, Oxford University Press, 2016, ISBN: 978–0–19–874855–7 (cit. on p. 10).

[26] *The SuperKEKB Accelerator*, URL:
https://www.belle2.de/en/belle-2-experiment/superkekb (visited on 11/05/2026) (cit. on p. 11).

[27] *SuperKEKB breaks new luminosity world record*,
URL: https://w3.lnf.infn.it/superkekb-breaks-new-luminosity-world-record/?lang=en (visited on 09/04/2026) (cit. on p. 12).

[28] Belle group, Physics Division I, KEK(High Energy Accelerator Research Organization), *Belle II Technical Design Report*, 2010, arXiv: 1011.0352 (cit. on pp. 12, 13).

[29] *The Belle II Detector*,
URL: https://www.belle2.de/en/belle-2-experiment/belle-ii-detector (visited on 20/04/2026) (cit. on pp. 12, 13).

[30] E. Kou and e. a. Urquijo, *The Belle II Physics Book*,
Progress of Theoretical and Experimental Physics **2019** (2019), ISSN: 2050-3911,
URL: http://dx.doi.org/10.1093/ptep/ptz106 (cit. on pp. 13, 19, 30).

[31] *PID (from a user's point of view)*,
URL: https://indico.belle2.org/event/7825/contributions/49614/attachments/19660/29149/PID%5C_tutorial%5C_v2.pdf (visited on 08/07/2026) (cit. on p. 15).

[32] *Belle II Software Documentation*,
URL: https://software.belle2.org/development/sphinx/index.html (visited on 15/06/2026) (cit. on pp. 16, 18–20, 25).

[33] N. G. e. a. The Belle Collaboration, *Study of decay mechanisms in $B^- -> \Lambda_c^+ \bar{p} \pi^-$ decay and observation of low mass structure in the $(\Lambda_c^+ \bar{p})$ system*, Physical Review Letters **97** (2006), ISSN: 1079-7114, URL: http://dx.doi.org/10.1103/PhysRevLett.97.242001 (cit. on p. 16).

[34] B. Aubert and Y. e. a. Karyotakis, *Observation of the baryonic B-decay $\overline{B}^0 \to \Lambda_c^+ \overline{p} K^- \pi^+$*, Phys. Rev. D **80** (5 2009) 051105(R),
URL: https://link.aps.org/doi/10.1103/PhysRevD.80.051105 (cit. on p. 16).

[35] Particle Data Group, K. Nakamura et al., *Review of Particle Physics*,
Phys. Rev. D **110** (3 2024) 030001, URL: http://pdg.lbl.gov (cit. on pp. 17, 27, 30).

[36] Keck, T., Abudinén, F., Bernlochner, F.U. et al, *The Full Event Interpretation*,
Comput Softw Big Sci **3** (2019), URL: https://doi.org/10.1007/s41781-019-0021-8 (cit. on p. 18).

[37] A. J. Bevan et al, *The Physics of the B Factories*, **74** (2014), arXiv: 1406.6311,
URL: http://dx.doi.org/10.1140/epjc/s10052-014-3026-9 (cit. on pp. 32, 33).

[38] *SysVar*, URL: https://sysvar.belle2.org/ (visited on 12/07/2026) (cit. on p. 34).

[39] A. L. Read, *Presentation of search results: the CLs technique*, **28** (2002) 2693, URL: https://doi.org/10.1088/0954-3899/28/10/313 (cit. on p. 38).

List of Figures

List of Tables

Acknowledgements

First and foremost, I would like to express my gratitude to my supervisors, Prof. Dr. Florian Bernlochner and Dr. Markus Prim, for giving me the opportunity to work on this exciting topic within the Belle II Collaboration. I am grateful for the continuous support and constructive feedback throughout the course of this thesis. Especially I would like to thank Dr. Markus Prim for the daily supervision, his patience and guidance in the development of this analysis and for always being there for all of my questions.

Furthermore, I would like to thank all members of the Belle II Collaboration for creating such an inspiring scientific environment and for developing and documenting the software, simulation framework and analysis tools on which this work is based on. In particular, I would like to thank Dr. Raynette Van Tonder and Verena Mendel from the Semileptonic Working Group in Karlsruhe for their close collaboration on this topic and for the helpful discussions and suggestions.

My sincere thanks go to my colleagues and fellow students in the working group here in Bonn for the amazing working atmosphere, their friendships and the interesting discussions during lunch and many coffee breaks. All of you made the board game evenings and other social events ensure that my time here was more than just work. A big thank you goes out to the people I shared an office with: Agrim Aggarwal, Melisa-Melek Akdag, Valerio Bertacchi and Nada Gharbi, who originally introduced me to this working group. I am very grateful for you helping me anytime I ran into problems or had a question, I could not have asked for better office mates.

Finally, I would like to thank my parents, my sister and my friends for their constant encouragement and support throughout my studies. Their confidence in me has given me a lot of energy and motivation during this journey.